

## 1      **Satellite Remote Sensing of Active Fires: History and 2      Current Status, Applications and Future Requirements**

3  
4      Wooster, M. J., Roberts. G. J., Giglio, L., Roy, D. P., Freeborn, P. H., Justice,  
5      C.O., Ichoku, C. M., Schroeder, W., Boschetti, L., Davies, D.K., Smith, A.M.S., Csiszar,  
6      I., Frost, P., Setzer, A., Zhang, T., de Jong, M.C., Johnston, J. M., Xu, W., Schmidt, C.,  
7      Strydom, T., Ellision, L., Vadrevu, K.P., Tanpipat, V., San-Miguel-Ayanz, J., Sparks,  
8      A.M., McCarty, J. L., Nguyen, H.

9  
10     Leverhulme Center for Wildfire, Environment & Society and NERC National Centre for  
11     Earth Observation (NCEO), c/o Dept. of Geography, Kings College London, Aldwych,  
12     London, WC2B 4BG, UK

13     [martin.wooster@kcl.ac.uk](mailto:martin.wooster@kcl.ac.uk)

14     University of Southampton, Geography and Environmental Science, Southampton, UK;  
15     [G.J.Roberts@soton.ac.uk](mailto:G.J.Roberts@soton.ac.uk)

16     Department of Geographical Sciences, University of Maryland, College Park, MD, USA  
17     [lgiglio@umd.edu](mailto:lgiglio@umd.edu)

18     Department of Geography, Environment, and Spatial Sciences, Michigan State  
19     University, East Lansing, MI, USA

20     [roydav1@msu.edu](mailto:roydav1@msu.edu)

21     Missoula Fire Sciences Laboratory, Rocky Mountain Research Station, USDA Forest  
22     Service, Missoula, MT, USA

23     [patrick.h.freeborn@usda.gov](mailto:patrick.h.freeborn@usda.gov)

24     Department of Forest, Rangeland, and Fire Sciences, , University of Idaho, Moscow, ID,  
25     USA

26     [luigi@uidaho.edu](mailto:luigi@uidaho.edu)

27     Department of Geographical Sciences, University of Maryland, College Park, MD, USA  
28     [cjustice@umd.edu](mailto:cjustice@umd.edu)

29     Interdisciplinary Studies, Atmospheric and Environmental Sciences, Howard  
30     University, Washington, District of Columbia, USA

31     [charles.m.ichoku@nasa.gov](mailto:charles.m.ichoku@nasa.gov)

32 NOAA/NESDIS/OSPO Satellite Analysis Branch, College Park, MD, USA  
33 [wilfrid.schroeder@noaa.gov](mailto:wilfrid.schroeder@noaa.gov)  
34 Trigg-Davies Consulting Ltd, Malvern UK /  
35 GSFC, Science Systems and Applications Inc, Lanham, Maryland United States  
36 [diane.k.davies@nasa.gov](mailto:diane.k.davies@nasa.gov)  
37 Department of Forest, Rangeland, and Fire Sciences, , University of Idaho, Moscow, ID,  
38 USA  
39 [alistair@uidaho.edu](mailto:alistair@uidaho.edu) [asparks@uidaho.edu](mailto:asparks@uidaho.edu)  
40 Centro de Previsão de Tempo e Estudos Climáticos/Instituto Nacional de Pesquisas  
41 Espaciais, Programa de Monitoramento de Queimada por Satélites, 12227-010, São José  
42 dos Campos, SP, Brazil  
43 [alberto.setzer@inpe.br](mailto:alberto.setzer@inpe.br)  
44 NOAA/NESDIS Center for Satellite Applications and Research (STAR), College Park,  
45 MD, USA  
46 [ivan.csizar@noaa.gov](mailto:ivan.csizar@noaa.gov)  
47 Scientific Services, South African National Parks, Skukuza, South Africa  
48 [tercia.strydom@sanparks.org](mailto:tercia.strydom@sanparks.org)  
49 iMMAP Middle East, Mecca St. 145, Amman, Jordan  
50 [pfrost@immap.org](mailto:pfrost@immap.org)  
51 Kings College London, Dept. of Geography, Strand, London, WC2R 2LS, UK  
52 NERC National Centre for Earth Observation (NCEO), Kings College London, UK  
53 [tianran.zhang@kcl.ac.uk](mailto:tianran.zhang@kcl.ac.uk)  
54 NERC National Centre for Earth Observation (NCEO), c/o. Dept. of Geography, Kings  
55 College London, Strand, London, WC2R 2LS, UK  
56 Kings College London, UK  
57 [weidong.xu@kcl.ac.uk](mailto:weidong.xu@kcl.ac.uk)  
58 NERC National Centre for Earth Observation (NCEO), c/o. Dept. of Geography, Kings  
59 College London, Strand, London, WC2R 2LS, UK  
60 [mark.dejong@kcl.ac.uk](mailto:mark.dejong@kcl.ac.uk)  
61 Canadian Forest Service, Great Lakes Forestry Centre, Sault Ste Marie, On. Canada  
62 [Joshua.Johnston@canada.ca](mailto:Joshua.Johnston@canada.ca)

63 Science Systems and Applications, Inc. (SSAI), NASA Goddard Space Flight Center,  
64 Greenbelt, MD 20771, USA.  
65 [lukecaj@gmail.com](mailto:lukecaj@gmail.com)  
66  
67 NASA Marshall Space Flight Center, Huntsville, Alabama, 35811, USA  
68 [krishna.p.vadrevu@nasa.gov](mailto:krishna.p.vadrevu@nasa.gov)  
69  
70 Department of Geography and Geospatial Analysis Center, Miami University, Oxford,  
71 OH, USA  
72 [mccartjl@miamioh.edu](mailto:mccartjl@miamioh.edu)  
73  
74 Upper ASEAN Wildland Fire Special Research Unit, Kasetsart University, Bkk, Thailand  
75 [fforvrc@ku.ac.th](mailto:fforvrc@ku.ac.th)  
76  
77 Cooperative Institute for Meteorological Satellite Studies, Space Science Engineering  
78 Center, University of Wisconsin-Madison  
79 [chris.schmidt@ssec.wisc.edu](mailto:chris.schmidt@ssec.wisc.edu)  
80  
81 European Commission Joint Research Centre, Ispra. [jesus.san-miguel@ec.europa.eu](mailto:jesus.san-miguel@ec.europa.eu)  
82

83

84 **Abstract**

85

86 Landscape fire is a widespread, somewhat unpredictable phenomena that plays an  
87 important part in Earth's biogeochemical cycling. In many biomes worldwide fire also  
88 provides multiple ecological benefits, but in certain circumstances can also pose a risk to  
89 life and infrastructure, lead to net increases in atmospheric greenhouse gas  
90 concentrations, and to degradation in air quality and consequently human health.  
91 Accurate, timely and frequently updated information on landscape fire activity is  
92 essential to improve our understanding of the drivers and impacts of this form of  
93 biomass burning, as well as to aid fire management. This information can only be  
94 provided using satellite Earth Observation approaches, and remote sensing of active fire  
95 is one of the key techniques used. This form of Earth Observation is based on detecting  
96 the signature of the (mostly infrared) electromagnetic radiation emitted as biomass  
97 burns. Since the early 1980's, active fire (AF) remote sensing conducted using Earth  
98 orbiting (LEO) satellites has been deployed in certain regions of the world to map the  
99 location and timing of landscape fire occurrence, and from the early 2000's global-scale

100 information updated multiple times per day has been easily available to all.  
101 Geostationary (GEO) satellites provide even higher frequency AF information, more  
102 than 100 times per day in some cases, and both LEO- and GEO-derived AF products  
103 now often include estimates of a fires characteristics, such as its fire radiative power  
104 (FRP) output, in addition to the fires detection. AF data provide information relevant to  
105 fire activity ongoing when the EO data were collected, and this can be delivered with  
106 very low latency times to support applications such as air quality forecasting. Here we  
107 summarize the history of achievements in the field of active fire remote sensing, review  
108 the physical basis of the approaches used, the nature of the AF detection and  
109 characterization techniques deployed, and highlight some of the key current capabilities  
110 and applications. Finally, we list some important developments we believe deserve focus  
111 in future years.

112

113

## 114 **1. Introduction**

115

116 Landscape fire is a widespread natural disturbance agent involved in Earth's  
117 biogeochemical cycling, but one that can be greatly influenced by human actions,  
118 including in relation to climate and environmental change. Fire provides multiple  
119 ecological benefits (McLauchlan et al., 2020) – but in certain circumstances also poses a  
120 risk to life and infrastructure (Duff and Penman, 2021). In areas of substantial  
121 landscape fire activity and in regions downwind, air quality can also be seriously  
122 degraded - leading to major human health impacts and hundreds of thousands of early  
123 deaths per year worldwide (Roberts and Wooster, 2021). Deforestation fires, other fire  
124 involving 'permanent' land cover conversion, and fires consuming peat soils can also  
125 result in a net release of carbon to the atmosphere, since unlike savannah or grassland  
126 fires the carbon released is not balanced by a roughly equivalent uptake over subsequent  
127 growing seasons (Sommers et al., 2014; Friedlingstein et al., 2020). Active fire (AF)  
128 remote sensing from space is a key technique used to deliver information on local to  
129 global scale fire activity for all these applications and more in a timely and accurate  
130 manner. Following a recent review of EO-based burned area mapping (Chuvieco et al.,  
131 2019), here we focus on EO for active fires – a technique that has developed to now

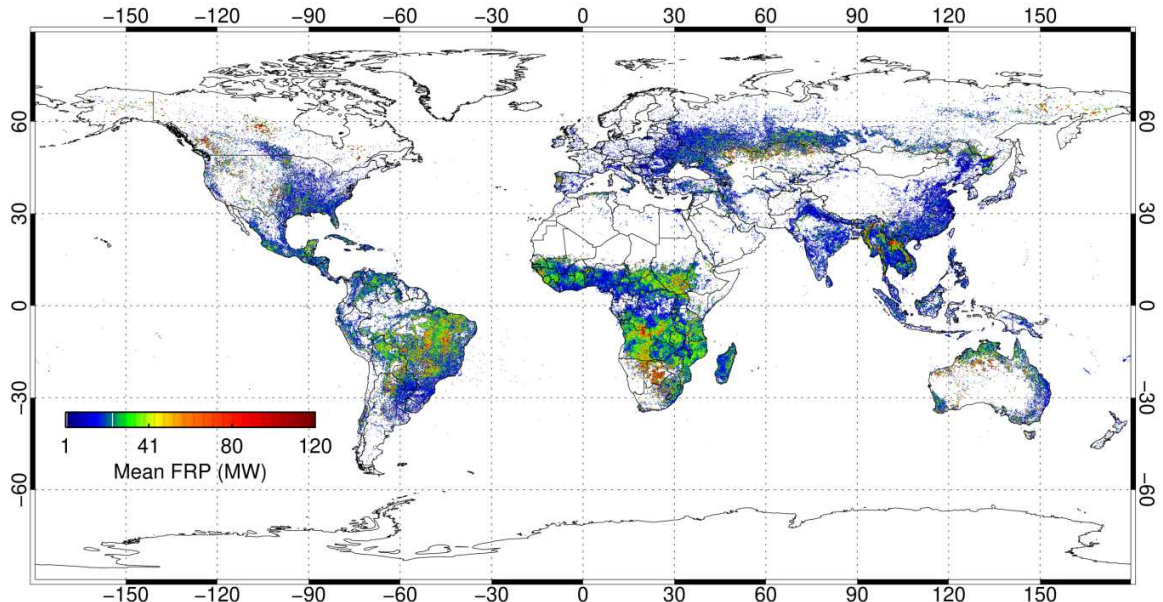
132 provide information on fire activity occurring anywhere on Earth with very low data  
133 latency and updates multiple times per day. Conducted as part of the Global  
134 Observation of Forest Cover/Global Observation of Landcover Dynamics  
135 (GOFC/GOLD) Fire Programme (<https://gofcgold.org/>), this review summarizes the  
136 history of the AF remote sensing approach, details current capabilities and key  
137 applications, and identifies important developments deserving focus in the coming  
138 years. Appendix 1 provides a glossary and acronym list covering many of the terms  
139 used, along with a definition of some of the most relevant physical and chemical  
140 quantities.

141 Figure 1 shows the annual distribution of actively burning landscape fires detected  
142 via processing of data collected by the Moderate Resolution Imaging Spectroradiometer  
143 (MODIS) instrument onboard NASA's Terra satellite. The fires detected include for  
144 example wildfires, those planned for some land management objective such as support  
145 to agriculture or forestry, and those used to clear land – including forests - for future  
146 agriculture. The data of Figure 1 clearly illustrate that widespread landscape fire activity  
147 occurs on all continents except Antarctica, generally in regions with enough dry fuel and  
148 ignition sources from people or lightning. Globally an average of around 3.4% of Earth's  
149 terrestrial surface area burns annually (Giglio *et al.*, 2018), an estimate that may  
150 increase as more finely detailed EO-derived burned area (BA) data become available  
151 (Roy *et al.*, 2019; Roteta *et al.*, 2019). Landscape fires such as these play important roles  
152 in many ecological (Bond and Keeley, 2005; McLauchlan *et al.*, 2020) and wider Earth  
153 system processes (Bowman *et al.*, 2009), including in relation to the carbon cycle  
154 (Sommers *et al.*, 2014). But their annual consumption of billions of tonnes of vegetation  
155 and organic soil also results in globally significant emissions of smoke to the atmosphere  
156 (van der Werf *et al.*, 2017), even from individual fire events (Hirsch and Koren, 2021),  
157 and this affects air quality (Jaffe *et al.*, 2020), and human health (Roberts and Wooster,  
158 2021). Those fires resulting in permanent landcover change, such as deforestation,  
159 and/or which consume carbon-rich organic soil such as peat built up over long-  
160 timescales also represent a net release of carbon to the atmosphere (e.g. Sommers *et al.*,  
161 2014; Huijnen *et al.*, 2015) and so contribute to rises in atmospheric greenhouse gas  
162 concentrations. One of the earliest stimuli for use of satellite EO in studying landscape  
163 fires came from uncertainties on their net carbon budget impact (Seiler and Crutzen,

164 1980), though a century earlier von Danckelman had drawn attention to their role in  
165 large-scale aerosol radiative forcing (Bronnimann *et al.*, 2009).

166 Satellite EO can be used to probe many fire characteristics, including burned area  
167 (Giglio *et al.* 2018; Chuvieco *et al.*, 2019) and the concentration and composition of  
168 smoke plumes (e.g. Kaufman *et al.*, 2002; Coheur *et al.* 2009; Ross *et al.*, 2013). Active  
169 fire (AF) remote sensing such as that used to produce the data of Figure 1 primarily  
170 focuses on identifying the location, timing and radiative strength (Fire Radiative Power;  
171 FRP) of fires that are actually consuming vegetation and/or organic soil at the time the  
172 observations were made. The FRP is somewhat akin to a spatial integration of the  
173 intensity of the overall combustion zone, and is measured in Watts. AF remote sensing  
174 is based primarily on infrared (IR) spectral measurements, and we begin by  
175 summarizing the historical development of the approaches used to exploit these  
176 measures (Section 2). We then review the fundamental physics (Section 3) and  
177 strategies for AF detection (Section 4), detailing approaches for FRP retrieval and the  
178 extraction of related variables such as fire effective temperature and area (Section 5).  
179 We examine how such data relate to fuel consumption and atmospheric impacts  
180 (Section 6), fire characteristics and ecosystem variables (Section 7), and how they are  
181 increasingly provided via online portals and in ‘analysis ready’ formats (Section 8).  
182 Finally, to aid future planning, we examine types of sensors, datasets and research  
183 activities we consider important for further development of AF applications, so as to  
184 point the way to areas of further fruitful research (Section 9).

185



186  
187

188 **Figure 1.** One year of actively burning landscape fire radiative power (FRP),  
189 derived from MODIS observations made from the Terra satellite. Data are the mean  
190 FRP of all active fire pixels detected in each  $0.5^{\circ}$  grid cell, as defined by the MODIS  
191 MCD14ML Active Fire and Thermal Anomaly product generated for 2010 (Giglio *et*  
192 *al.*, 2016).

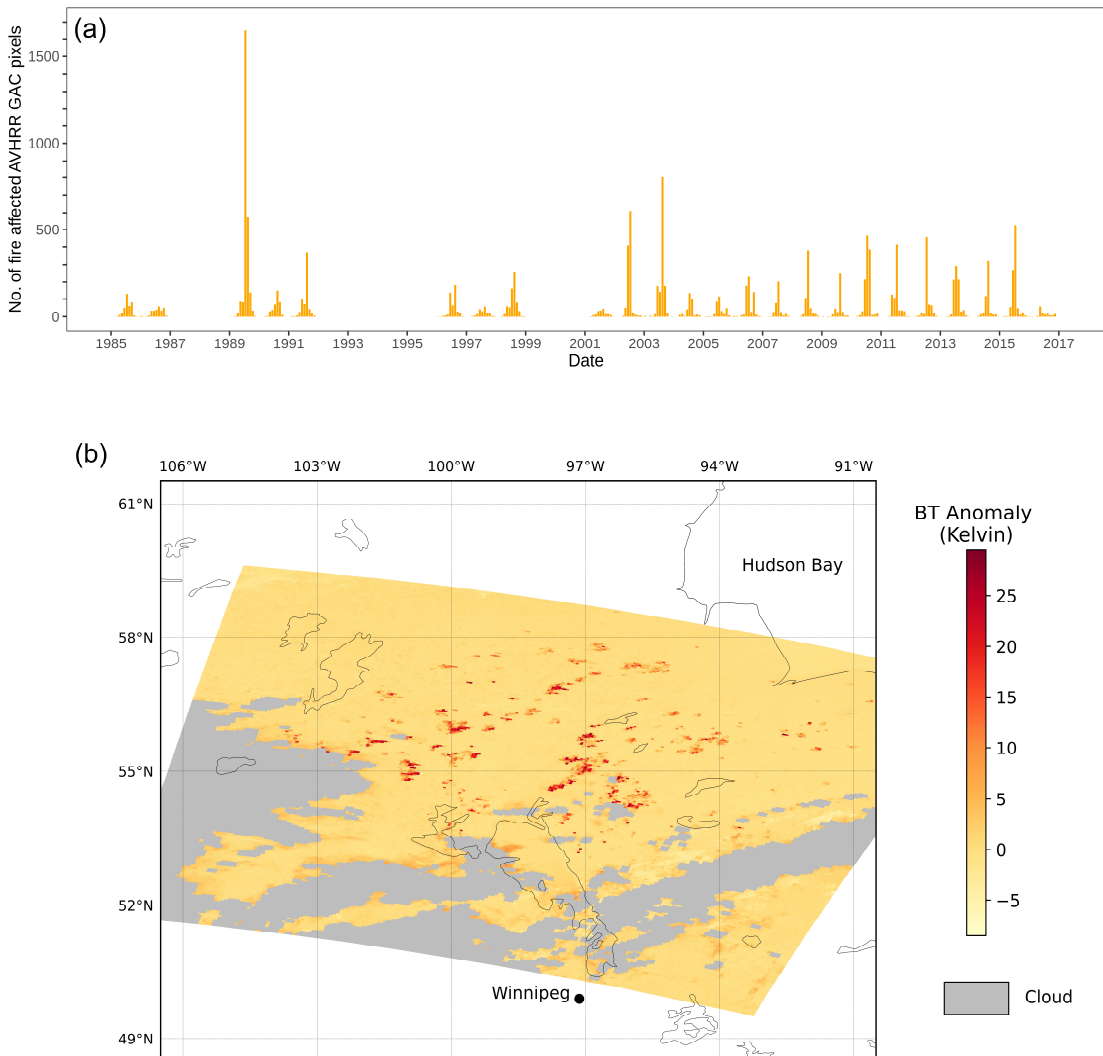
193

## 194 **2. The Historical Development of Satellite Active Fire (AF) Methods**

195

196 The origins of active fire remote sensing extend back to 1960's and 1970's, with  
197 airborne thermal imaging of forest and coal seam fires (e.g. Hirsch, 1965; Ellyett and  
198 Flaming, 1973). Satellite-based studies commenced in the early 1980's, primarily using  
199 data from the Advanced Very High Resolution Radiometer (AVHRR) operating onboard  
200 NOAA's Polar-orbiting Operational Environmental Satellites (POES). AVHRR data  
201 played a key role in the development of AF detection methods (e.g., Flasse and Ceccato,  
202 1996; Giglio *et al.* 1999; Ichoku *et al.*, 2003). Research was largely based on the strong  
203 'active fire sensitivity' of spectral bands located in the middle infrared (MIR)  
204 atmospheric window ( $3 - 5 \mu\text{m}$ ) (Section 3), with the AVHRR  $3.7 \mu\text{m}$  channel shown to  
205 discriminate areas of combustion covering  $< 1\%$  of the pixel area (Dozier; 1981; Matson  
206 and Dozier, 1981; Muirhead and Cracknell, 1985; Flannigan and Vonder Haar, 1986; Lee

207 and Tag, 1990; Setzer and Periera, 1991; Justice *et al.*, 1993). The sensitivity of MIR  
208 measurements to sub-pixel thermal anomalies still underpins most AF remote sensing  
209 today, and AVHRR itself is still used (e.g., in the Brazilian ‘Queimadas’ fire monitoring  
210 system described in Appendix 2). During the 1980’s the first AVHRR-based active fire  
211 initiatives were unable to use the full spatial resolution (1 km) data globally due to the  
212 limited ‘local area coverage’ (LAC) onboard storage capacity of POES. However, a global  
213 network of AVHRR ground stations collected the directly downlinked High Resolution  
214 Picture Transmission (HRPT) 1 km data broadcast from the POES within their coverage  
215 areas, and in 1992 the International Geosphere Biosphere Programme Data and  
216 Information System (IGBP-DIS) provided specifications for the first global 1 km data set  
217 (Eidenshink and Faundeen 1994). This led to the first ever day and night global AF data  
218 set, produced by Europe’s Joint Research Center (JRC; Ispra) covering April 1992 to  
219 December 1993 (Stroppiana *et al.* 2000). The nighttime only ESA World Fire Atlas  
220 (WFA) was developed at a similar time using initially ATSR-2 observations (Arino *et al.*,  
221 1999). The call for such global fire products originated in the requirements set by the  
222 IGBP Global Change and Terrestrial Ecology (GCTE) Core Project and the response by  
223 IGBP Data and Information Systems (IGBP-DIS), and was taken up more  
224 comprehensively by the international community through the GOFC/GOLD program  
225 (Ahern *et al.*, 2003, Csiszar *et al.* 2013). Most recently the nearly 40-year archive of  
226 global, lower ( $\sim 3 \times 5$  km) spatial resolution subsampled AVHRR global area coverage  
227 (GAC) data has been mined to generate some of the longest AF records currently  
228 available, initially regionally (e.g. Wooster *et al.*, 2012a) and now being extended  
229 globally. **Figure 2** shows an example of a three-decade AVHRR-GAC AF analysis of  
230 southern Canadian provinces (**Figure 2a**), where extreme fires burned in Manitoba in  
231 May, July and August 1989 (**Figure 2b**).



235      **Figure 2.** Example of (a) long term and (b) extreme landscape fire activity  
 236      recorded in southerly Canadian provinces, as depicted via analysis of AVHRR GAC  
 237      data. (a) AF detection time series derived using nighttime GAC data from 1985 to  
 238      2016. (b) Example AVHRR GAC image of 24<sup>th</sup> July 1989 (09:00 UTC) taken during  
 239      the extreme 1989 Manitoba fire season (see the peak in (a) and Hirsch, 1991). Cloudy

240 pixels are masked as grey and active fire pixels shown by the high MIR (3.7  $\mu\text{m}$ )  
241 channel brightness temperature elevation over the ambient background (red areas).

242

243

244 Work with AVHRR fundamentally changed our understanding of the global  
245 presence of fire, but the low sensor saturation temperature (c. 325K) of AVHRRs 3.7  
246  $\mu\text{m}$  MIR band (Csiszar and Sullivan, 2002), significant POES orbital drift (Csiszar *et*  
247 *al.* 2003) as well as other issues (Giglio and Roy, 2020) provided limits to its utility.  
248 However, such work greatly influenced the presence of an AF detection and  
249 characterization capability within NASA's Earth Observing System (EOS; Justice *et al.*,  
250 1998), specifically that of the EOS flagship sensor - MODIS (Justice *et al.* 2002a).  
251 MODIS was designed with two 3.96  $\mu\text{m}$  MIR channels having different saturation  
252 temperatures and dynamic ranges to support FRP retrieval as well as AF detection  
253 (Kaufman *et al.*, 1998; Justice *et al.* 2002b). FRP retrieval (Section 5) enables the AF  
254 application to go beyond fire presence/absence mapping to quantify the amount of  
255 radiant energy a fire is emitting per unit time, which is now considered linearly related  
256 to rates of fuel (vegetation and/or organic soil) consumption and smoke emission (e.g.  
257 Kaufman *et al.*, 1996; Ichoku and Kaufman, 2005; Wooster *et al.*, 2005; Kaiser *et al.*,  
258 2012; Nguyen and Wooster, 2021). The MODIS AF detection algorithms were built on  
259 the AVHRR experience and prototyped using MODIS airborne simulator data  
260 (Kaufman *et al.*, 1998). They exploited the increased brightness temperature (BT)  
261 difference found between the MIR and long-wave infrared (LWIR) channel  
262 measurements at pixels containing actively burning fires (Section 3). The MODIS AF  
263 detection algorithm (Section 4) has been used by NASA to generate a suite of AF  
264 products having better than daily temporal resolution since the year 2000, and these  
265 remain to the present time one of the most widely used MODIS products. Other  
266 satellites in the 1990's and 2000's also supported AF detection, including the Defense  
267 Meteorological Satellite Program nighttime low-light imaging Operational Linescan  
268 System (DMSP-OLS) (e.g. Cahoon *et al.*, 1992; Elvidge *et al.*, 2013) and the Tropical  
269 Rainfall Mapping Mission (TRMM) which relied on evolutions of AF detection  
270 methods first used with AVHRR (e.g. Giglio *et al.*, 2000).

AF detection accuracy assessment is challenging due to the ephemeral and highly dynamic nature of landscape fire, difficulties in obtaining independent reference data coincident with the satellite observations, and because surface fires are complex to characterize *in situ*. However, for MODIS, the inclusion of the higher spatial resolution (15, 30 and 90 m) Advanced Spaceborne Thermal Emission and Reflection Radiometer (ASTER) instrument operating concurrently on the Terra satellite and itself able to be used for AF detection enabled simultaneous reference data to be collected. A systematic evaluation of the minimum fire sizes detectable by MODIS was produced (Morisette *et al.*, 2005; Schroeder *et al.*, 2008), and further refinements to the MODIS AF detection algorithm were informed by this validation. This culminated in the latest Collection 6 dataset reprocessing (Giglio *et al.*, 2016). These developments also influenced algorithms used with subsequent low earth orbit (LEO) satellite sensors, such as the Visible Infrared Imaging Radiometer Suite (VIIRS) (Csiszar *et al.*, 2014) and Sentinel-3 Sea and Land Surface Temperature Radiometer (SLSTR) (Wooster *et al.*, 2012b; Xu *et al.*, 2020). Inter-comparisons of AF data derived from observations made by different LEO sensors are commonly used to understand their varying performance characteristics (**Figure 3**), with one aim being to derive transfer functions enabling data from multiple sensors to be combined into single time-series.

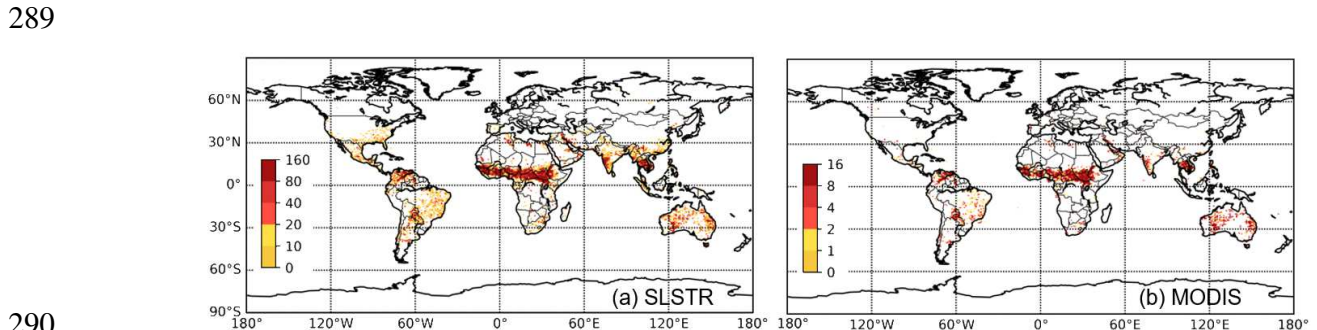


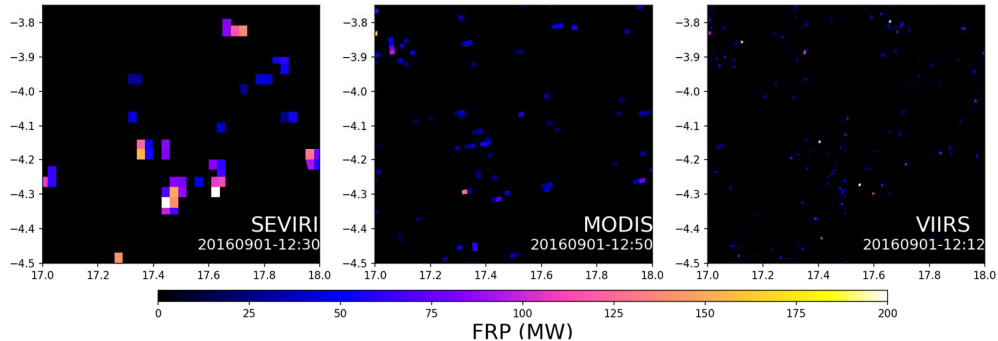
**Figure 3.** Nighttime active fire pixel counts detected in 0.1° grid cells in January 2019 from (a) Sentinel3B SLSTR and (b) Terra MODIS. These sensors have similar local overpass times and show similar spatial patterns of AF detection, but the SLSTR data record shows far higher AF pixel counts. Analysis shows this is in part due to the detection of many lower FRP fires by SLSTR than MODIS. This is a result of the former sensors smaller pixel area growth around the swath compared to MODIS (Wooster *et*

298 *al.*, 2012a; Xu *et al.*, 2020), and the fact that lower FRP fires are typically the most  
299 numerous (e.g. Wooster and Zhang, 2004).

300

301 A similar AF detection algorithm development cycle has occurred for geostationary  
302 (GEO) satellite AF products as with LEO products. Compared to LEO systems, GEO  
303 products offer higher temporal resolutions but coarser spatial resolutions, and each  
304 sensor only provides data over a specific region of the Earth (**Figure 4**). Geostationary  
305 AF products were first generated over the America's using the Geostationary  
306 Operational Environmental Satellite Visible Infrared Spin Scan Radiometer  
307 Atmospheric Sounder (GOES-VAS) (e.g. Prins and Menzel, 1992; 1994; Weaver *et al.*,  
308 1995), and this led to the development of the long-standing GOES WildFire Automated  
309 Biomass Burning Algorithm (GOES WFABBA) product (Prins *et al.*, 1998). The GOES  
310 WFABBA products represent the longest geostationary AF dataset currently available,  
311 and in addition to AF location and time included an estimate of effective AF  
312 temperature and area - derived using the Dozier (1981) 'bi-spectral' approach (Section  
313 4). Wooster *et al.* (2005) and Roberts *et al.* (2005) first demonstrated the retrieval of  
314 FRP from geostationary EO data, doing so via an approach avoiding use of bi-spectral  
315 data (see Section 5), and went on to develop a full 'fire thermal anomaly' (FTA) AF  
316 detection and FRP retrieval algorithm for GEO systems. This was first applied to data  
317 from Meteosat Second Generation (Roberts and Wooster, 2008), and an operational  
318 version is now used to generate a series of geostationary AF detection and FRP retrieval  
319 products spanning much of the globe, including from Meteosat over Africa and Europe  
320 (Wooster *et al.*, 2015), GOES-East and -West over the America's (Xu *et al.*, 2010; 2021)  
321 and Himawari over Asia (Xu *et al.*, 2017). Similar product intercomparisons and  
322 evaluations have been conducted as for LEO AF products (e.g. Roberts *et al.*, 2015).

323



324

325

326

327

328

329

330

331

332

333

334

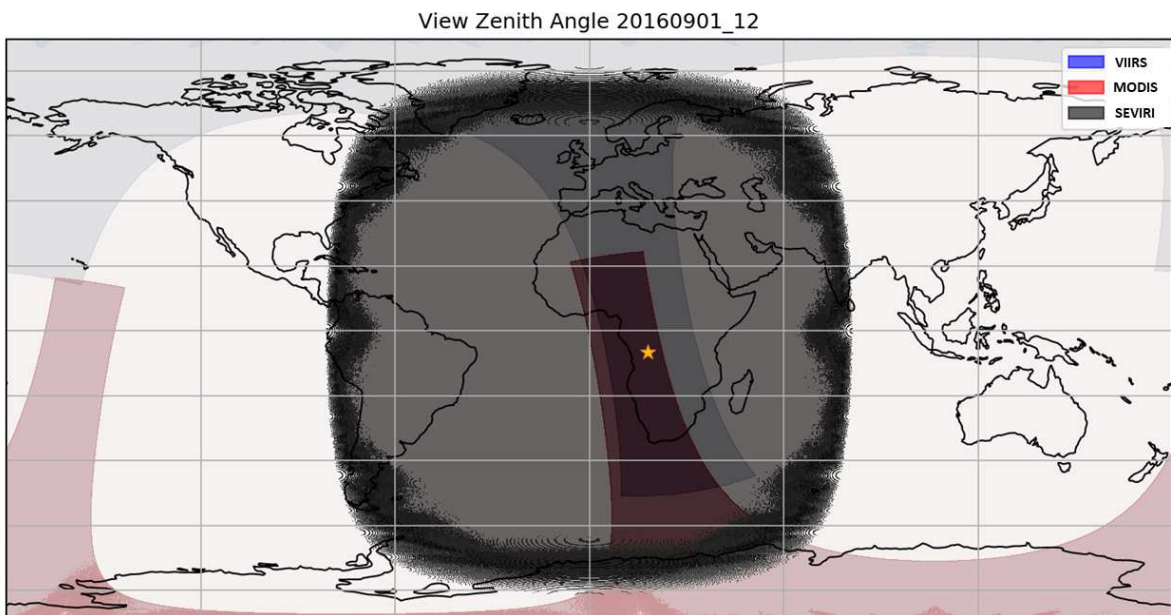


**Figure 4.** Active fire data and coverage maps derived from observations made by the geostationary Meteosat Second Generation SEVIRI instrument (SEV), and the polar-orbiting Aqua MODIS (MYD) and VIIRS (VNP) at approximately the same time of day. An approximately  $80 \times 100$  km region of southern Africa is shown at top, where the coarser spatial detail of SEVIRI is apparent but also the higher per pixel FRP values due to the capturing of more fires within a pixel. The spatial

335 coverage of each of these systems obtained in a single hour is shown in the global  
336 map, with the location of the focus region highlighted.

337

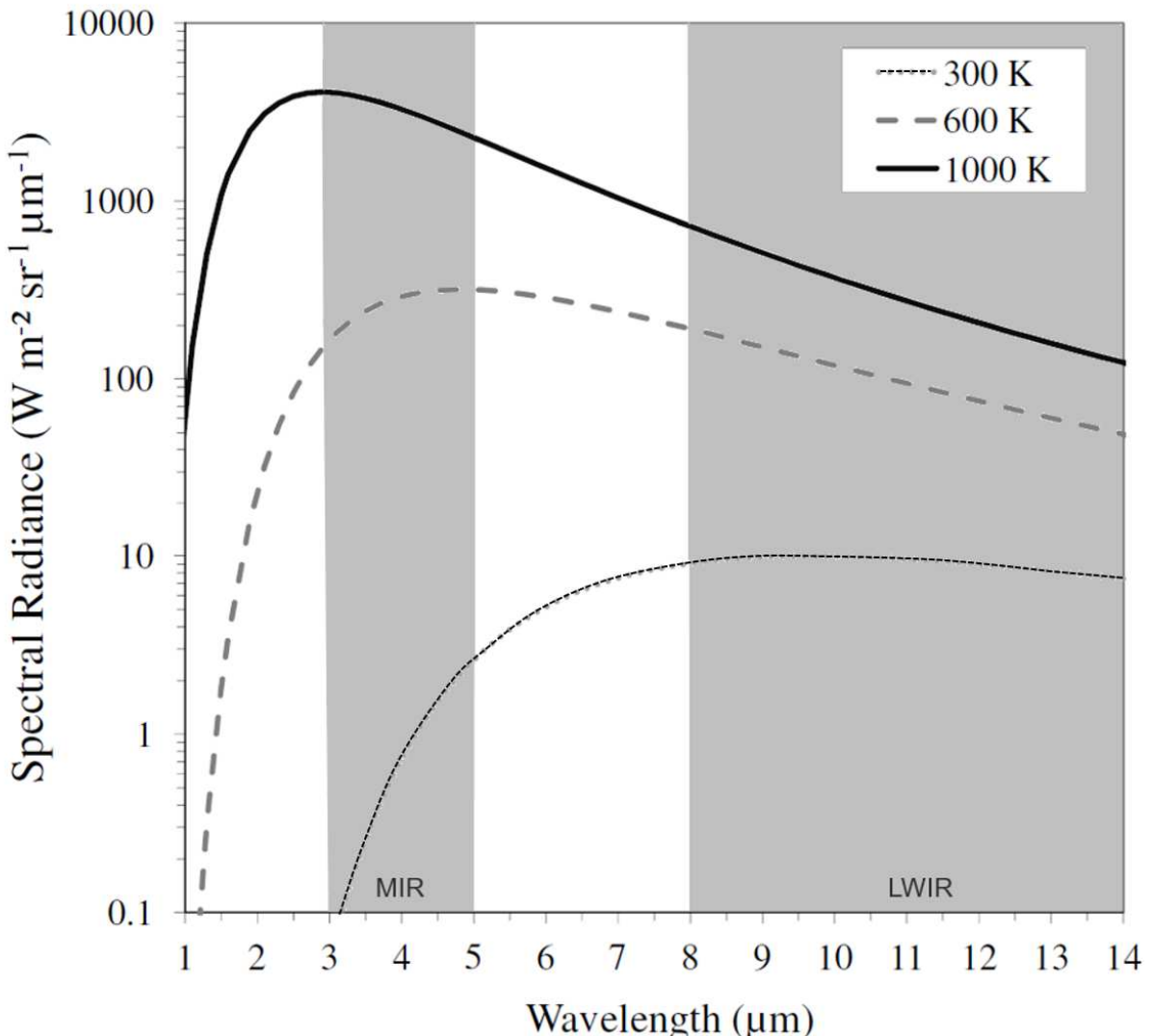
### 338 **3. Basic Physics of Active Fire Remote Sensing**

339

340 AF detection and characterization is based on remote sensing of some of the  
341 approximately 20 MJ.kg<sup>-1</sup> of energy released when vegetation and organic soil burns  
342 (Cheney and Sullivan, 2008). ‘High heat of combustion’ describes the maximum total  
343 energy release per unit of dry matter consumed, and so live, i.e., moist, fuels release  
344 somewhat less (Smith *et al.*, 2013). Of the total energy released, only about 10 - 20% is  
345 released as (primarily IR) electromagnetic radiation (Freeborn *et al.* 2008, Kremens *et*  
346 *al.*, 2012). This radiative energy release rate is far higher than from the same area of  
347 ambient land however, and its spectral distribution follows Planck’s Radiation Law and  
348 its derivative Wien’s Displacement Law which serve as the physical basis for most AF  
349 remote sensing.

350

351 **Figure 5** shows the modeled blackbody emitted spectral radiance for surfaces at 300 K,  
352 600 K and 1000 K (typical temperatures of the Earth’s land surface, smoldering, and  
353 flaming combustion respectively; Kaufman *et al.* 1998; Sullivan *et al.* 2003; Dennison *et*  
354 *al.* 2006). The emitted spectral radiance from a 1000 K flaming fire in the longwave IR  
355 (LWIR) atmospheric window (8 – 14 µm) is more than an order of magnitude higher  
356 than from the ambient land surface, but in the MIR (3 – 5 µm) atmospheric window it is  
357 almost three orders of magnitude higher – demonstrating why MIR observations are so  
358 sensitive to the presence of actively burning fires. Cooler smoldering fires show lower  
359 but still very significant levels of MIR and LWIR emittance. The very strong radiative  
360 signal of areas of combustion in the MIR spectral region, and the contrast between this  
361 and that seen in the LWIR from the same location, and in the MIR from nearby ambient  
362 non-fire areas, mean that active fires can be detected in appropriately remotely sensed  
363 imagery even if they cover an extremely small fraction of a pixel.



366  
367 **Figure 5.** Emitted spectral radiance for blackbodies at typical flaming (1000 K) and  
368 smoldering (600 K) temperatures along with that from an ambient 300 K surface.  
369 Note the logarithmic scale of the y-axis. The MIR and LWIR atmospheric window  
370 regions are shaded grey.

371  
372 To demonstrate that even small sub-pixel fires generate very detectable changes in the  
373 signal of the pixels they are contained within, **Figure 6** shows an example of modelled  
374 top-of-atmosphere (TOA) spectral radiance for different pixel situations, fully taking  
375 into account both emitted and reflected radiation and atmospheric effects. The figure  
376 contrasts a 300 K savannah land surface pixel (green line) with the same pixel but also

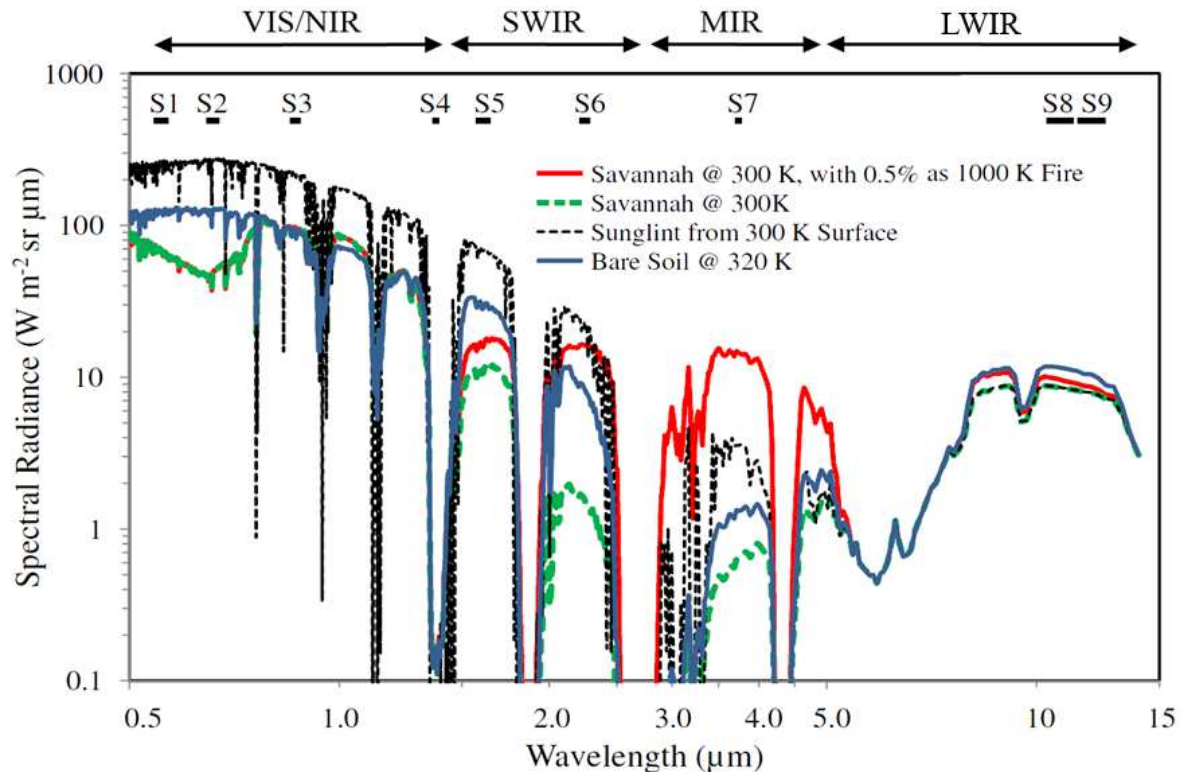
377 containing 0.5 % areal coverage of flaming 1000 K combustion (red line). In the MIR  
378 spectral region (3 – 5  $\mu\text{m}$ ), there is around an order of magnitude difference between the  
379 spectral radiance of these two pixels, equivalent to an easily detectable brightness  
380 temperature (BT) difference of around 80 K - even though the fire covers less than 1% of  
381 the pixel area. Whilst there is a dependency on issues such as day/night operation, and  
382 certain instrument-specifics, most AF detection algorithms can identify pixels in  
383 remotely sensed imagery that contain active fires if they have induced a minimum 5 to  
384 10 K increase in the pixels MIR brightness temperature compared to the non-fire  
385 background. As such, fires covering down to perhaps  $\sim 0.01\%$  of the pixel area are  
386 potentially identifiable. A far lower (but still likely detectable) signal difference between  
387 the fire and non-fire savannah pixels is apparent in the 10 – 12  $\mu\text{m}$  LWIR spectral region  
388 of **Figure 6**, indicating that fires essentially have to cover a far larger portion of the  
389 pixel area to be identified using LWIR observations than MIR observations. These types  
390 of spatial and spectral contrast differences are the basis of most AF detection  
391 algorithms, with various additional tests employed to discriminate AF pixels from 'false  
392 alarms'. Pixels containing homogeneously warm (e.g. solar heated) land would be  
393 expected to have more similar MIR and LWIR BTs than would AF pixels, enabling the  
394 latter to be discriminated using this characteristic (see Section 4), whilst geographic  
395 masks can be used to screen out land-based gas flaring and active volcanoes for  
396 example.

397  
398 Figure 6 also shows the signal of a pixel containing sunglint over water, which is a key  
399 cause of potential false alarms since sunglint affected pixels can have similar MIR and  
400 LWIR signals to AF pixels. However, sun glints can be masked out based on their  
401 typically strong visible wavelength and/or near infrared (NIR) signals (e.g. Zhukov *et*  
402 *al.*, 2006). Sunglint does not occur at night, and so nighttime AF detection algorithms  
403 can often be deployed with increased sensitivity, including because nighttime ambient  
404 surface temperatures are typically lower and more homogeneous than by day - leading  
405 to potential increases in the contrast provided by AF pixels. Some nighttime AF  
406 detection algorithms employ analysis of short-wave infrared (SWIR) signals (typically  
407 between 1.6 and 2.2  $\mu\text{m}$ ), which Figure 5 and 6 shows are also raised by the presence of

408 sub-pixel active fires. By day however such emitted SWIR signals can be masked by  
 409 variations in solar reflected radiation unless the fire covers a substantial fraction of the  
 410 pixel area. Such methods are thus best suited to use with higher spatial resolution  
 411 imagery (e.g. Giglio et al., 2008).

412

413



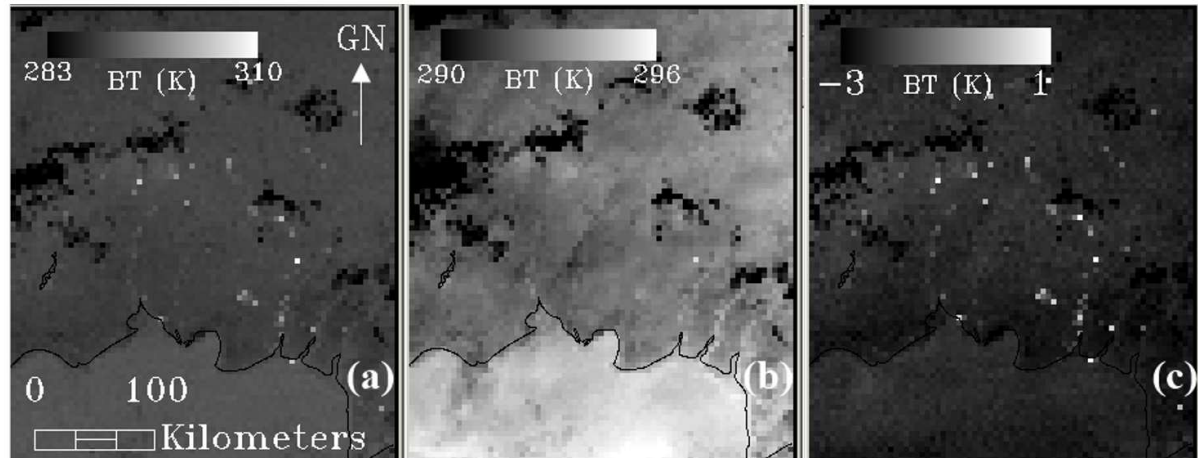
414

415

416 **Figure 6.** Modeled top-of-atmosphere emitted spectral radiance for four pixels –  
 417 containing ambient (300 K) savannah; the same but with a 1000 K actively burning  
 418 fire covering 0.5% of the pixel area, specularly-reflected sunglint from a 300 K  
 419 surface, and solar-heated bare soil at 320 K. Examples of typical spectral bands of a  
 420 satellite based imaging radiometer used to detect AF pixels are shown at top (here  
 421 those from the Sentinel-3 SLSTR sensor; Wooster *et al.*, 2012a). Savannah pixels  
 422 which contain a sub-pixel active fire are best separated from non-fire pixels in MIR  
 423 spectral region, which is targeted by the SLSTR S7 spectral band. SLSTR also has a  
 424 second (low-gain) MIR band (F1) to avoid saturation effects that impact S7 over  
 425 warmer areas and active fires (see Section 10).

426

427 Few active fires completely fill a satellite image pixel, and extremely rarely at the  
 428 scale of MODIS, SLSTR and VIIRS pixels. Thus subpixel AF situations such as is  
 429 modelled in Figure 6 are by far the most common type. However, reliable detection of  
 430 extremely small subpixel (e.g. < 0.01% pixel area), sub-canopy smouldering, or  
 431 particularly cool (e.g. subsurface peat) fires remains a challenge. A fire of a given size  
 432 and temperature will also occupy a smaller areal fraction of a larger pixel than a smaller  
 433 pixel, reducing its detection reliability. However, moderate spatial resolution EO data  
 434 such as provided by AVHRR, MODIS, VIIRS, and SLSTR are available with a daily or  
 435 better update frequencies, enabling detection of active fires covering around 100 m<sup>2</sup> and  
 436 in some cases even smaller (Schroeder *et al.*, 2014; Zhang *et al.*, 2017). **Figure 7** shows  
 437 an AVHRR 1 km image captured over Indonesia during a period when flaming  
 438 vegetation fires and cooler (often sub-surface) smouldering peat fires were widespread.  
 439 These fires are generally strongly sub-pixel in size, and in agreement with **Figures 5**  
 440 and **6** their influence on the MIR BT image (a) is far greater than in the LWIR BT image  
 441 (b). The BT difference image (**Figure 7c**) best highlights the AF pixels, and this  
 442 difference metric is the basis of most AF detection algorithms (Section 4).  
 443



444

445

446 **Figure 7.** Night-time AVHRR local area coverage (LAC) ~ 1 km spatial resolution  
 447 imagery of large-scale fires burning in primarily in peatlands across southern  
 448 Kalimantan (Indonesia) on 24<sup>th</sup> August 1991. (a) MIR and (b) LWIR brightness

449 temperature (BT) data. The presence of a sub-pixel fire affects the BT more in the MIR  
450 than in the LWIR, and the MIR and LWIR BT difference shown in (c) most clearly  
451 highlights them.

452

453 **Figure 7** shows a largely cloud free situation. Unlike smoke, meteorological clouds  
454 obscure active fires from view, and can also contribute to sunglint-induced false alarms.  
455 Cloud masking is thus an important component of EO-based AF detection. Information  
456 on cloud masked areas is also essential for AF product users to understand whether a  
457 location is considered free of detectable fires, or whether there is uncertainty due to  
458 cloud cover. Atwood *et al.* (2015) demonstrate that AF detection can occur through even  
459 very thick smoke, but that some satellite AF product cloud masking procedures  
460 inadvertently mask out heavily smoke affected areas as being affected by cloud.  
461 Conservative cloud masks can also result in higher rates of AF omission, and so  
462 underestimation of regional-scale FRP totals (Freeborn *et al.*, 2014; Hall *et al.*, 2019;  
463 Liu *et al.*, 2020). However, Wooster *et al.*, (2018) demonstrate that considerable  
464 spatio-temporal detail on fire activity in strongly smoke and cloud affected regions can  
465 still be gained with suitable tailoring of AF product cloud masking procedures.

466

467 To aid understanding of the exact source of the types of elevated spectral signals  
468 shown in **Figure 6** over fire affected pixels, Parent *et al.* (2010) made high spectral  
469 resolution laboratory measurements of fire emitted radiation. Planckian thermal  
470 emission was seen coming from both the hot fuel and from luminous hot soot particles  
471 in the flames, but whilst the fuel typically had a high emissivity across the IR region,  
472 that of the flames depended strongly on soot concentration and flame depth (Àgueda *et*  
473 *al.*, 2010; Johnston *et al.* 2014). However, even in low emissivity (e.g. thin, low soot  
474 concentration) flames showing low amounts of Planckian thermal emission, strong  
475 thermal emission in narrow spectral ‘emission line’ regions were seen from hot gases  
476 such as CO<sub>2</sub> and H<sub>2</sub>O (Parent *et al.*, 2010). EO sensors prioritized for AF remote sensing  
477 generally avoid use of such spectral regions however, since ambient atmospheric CO<sub>2</sub>  
478 and H<sub>2</sub>O absorb strongly at these same wavelengths and would tend to obscure the  
479 surface emitted signals when observing from space. Atmospheric transmittance is taken  
480 into account of during the generation of certain AF products, but typically only in terms

481 ambient atmospheric gaseous constituents (e.g. Wooster *et al.*, 2015; Section 5). In  
482 terms of aerosols, wildfire smoke is dominated by very small particles (i.e. PM2.5 and  
483 smaller) that are inefficient scatterers of MIR and LWIR radiation, and this is the reason  
484 that fires can be identified though even strongly smoke-affected regions as long as the  
485 data are not masked as cloudy (Atwood *et al.*, 2015). However, thick smoke is likely to  
486 have some impact on the retrieved FRP, including via any black carbon component  
487 absorbing some of the fire-emitted thermal radiance. This is yet to be accounted for in  
488 FRP retrieval algorithms.

489

## 490 **4. Active Fire Detection Algorithms and Products**

491

### 492 **4.1. Active Fire Detection Algorithms**

493

#### 494 **4.1.1 Early Work**

495

496 Dozier (1981) and Matson and Dozier (1981) undertook some of the earliest  
497 satellite-based studies of sub-pixel ‘thermal anomalies’. They explained the causes of the  
498 spectrally varying BTs seen in AVHRR data containing sub-pixel hot sources (e.g. Figure  
499 7), and these characteristics still underly almost all AF detection methods used today.  
500 They proposed a so-called bi-spectral fire characterisation algorithm that used non-  
501 linear simultaneous equations to estimate the fires sub-pixel effective temperature and  
502 area (see Section 5.1). Prior to application of this bi-spectral, other approaches are often  
503 used to identify the pixels to which it should be applied.

504

#### 505 **4.1.2 Fixed threshold algorithms**

506

507 Fixed threshold AF detection algorithms apply relational operators and fixed  
508 thresholds to the BT data captured in individual spectral bands (e.g.,  $T_{MIR} > 320K$ )  
509 and/or to band differences (e.g.,  $T_{MIR} - T_{LWIR} > 10 K$ ). Their simplicity provides  
510 computational efficiency, but even carefully-tuned thresholds can in general only satisfy  
511 AF detection accuracy requirements under the specific regional/seasonal conditions for  
512 which they were derived (Kaufman *et al.*, 1990; Pereira and Setzer, 1993), or they must

513 be applied under relatively stable ambient background temperature conditions (e.g. at  
514 night; Wooster *et al.*, 2012b). Use of higher thresholds can help alleviate false alarms  
515 related to by ambient background temperature variations, as was the case with the ESA  
516 World Fire Atlas, but increase the chance of omitting smaller and/or cooler fires (Arino  
517 *et al.*, 1999).

518

#### 519 **4.1.3 Contextual algorithms**

520

521 Contextual algorithms incorporate dynamic thresholds, which adapt to local  
522 conditions to aid detection of smaller and/or cooler fires whilst minimizing false alarms.  
523 In this approach, candidate AF pixels are first detected using liberal fixed thresholds -  
524 generally applied to the  $T_{MIR}$  and/or  $T_{MIR} - T_{LWIR}$  data. False detections are then  
525 removed from this 'potential AF pixel' set by comparing the signal of each candidate AF  
526 pixel to that of neighboring non-fire pixels within a surrounding geographic window.  
527 Some of the first contextual AF detection algorithms were developed for use with  
528 AVHRR (e.g. Flasse and Cecatto (1996); Giglio *et al.*, 1999) as part of the IGBP-DIS  
529 global fire initiative (Section 2). Evolutions followed, including use of differently sized  
530 windows (e.g. Giglio *et al.*, 2003, 2016; Zhukov *et al.*, 2006), and spatial filters to  
531 improve rejection of non-fire pixels in the early stages and allow use of more liberal  
532 fixed thresholds able to better capture smaller/coolier fires (Roberts and Wooster,  
533 2008).

534 Contextual algorithms still remain the most commonly used AF detection  
535 method. Since their initial development (Flasse and Ceccato, 1996; Giglio *et al.*, 1999;  
536 Kaufman *et al.*, 1998), they have been applied to data from numerous LEO sensors,  
537 including VIIRS (Schroeder *et al.*, 2014; Csiszar *et al.*, 2014; Zhang *et al.*, 2017), MODIS  
538 (Kaufman *et al.*, 1998; Giglio *et al.*, 2016), the BIRD Hot Spot Recognition System  
539 (HSRS, Zhukov *et al.*, 2006), the TRMM Visible and Infrared Scanner (VIRS, Giglio *et*  
540 *al.*, 2000), SLSTR (Wooster *et al.*, 2012b; Xu *et al.*, 2020), and Landsat (Schroeder *et al.*  
541 2016; Kumar and Roy, 2018), and also GEO sensors such as those carried by Meteosat  
542 (e.g. Wooster *et al.*, 2015; Amraoui *et al.*, 2010; Di Biase and Laneve, 2018), GOES  
543 (Prins *et al.*, 1998; Xu *et al.*, 2010; Schmidt *et al.*, 2017; Xu *et al.*, 2021), Himawari (Xu  
544 *et al.*, 2017; Wickramasinghe *et al.*, 2016), and FengYun (Xu *et al.*, 2011).

545

546 **4.1.4 Multi-temporal algorithms**

547

548 The majority of AF detection algorithms are applied to single date imagery, with  
549 some adding basic temporal constraints to remove possible false alarms (e.g., Prins *et*  
550 *al.*, 1998; Xu *et al.*, 2010; Kumar and Roy, 2018). Some multi-temporal AF detection  
551 algorithms have been developed however. These either identify fire-related pixel-level  
552 thermal variations via multi-temporal change detection (e.g. Filizzola *et al.*, 2017), or  
553 model the ambient pixel BT diurnal cycle and identify fire-related departures from this  
554 (e.g. Roberts and Wooster, 2014). Both approaches aim to identify an AF pixel via  
555 thermal differences compared to expectations, whilst accounting for temporal  
556 variability. In the multi-temporal change detection approach, statistical  
557 characterizations of a fire-relevant parameter (e.g., the MIR BT or MIR-LWIR BT  
558 difference) at each pixel location are calculated over a suitably long period; and such  
559 approaches have been applied to LEO (Marchese *et al.*, 2017) and GEO (Laneve *et al.*  
560 2006; Filizzola *et al.*, 2017) data. Model-based approaches exploit the latter's higher  
561 temporal frequency to characterize the ambient BT diurnal cycle and then forecast this  
562 forward in time (Udahemuka *et al.*, 2007; Hally *et al.*, 2017). Optimal estimation  
563 techniques, such as Kalman filters, can build on this baseline to assimilate observed BTs  
564 and deploy statistical thresholds to confirm whether active fires are present based on  
565 departures from the modelled diurnal trend. Although computationally intensive, this  
566 approach has been applied to GEO data (van den Bergh and Frost, 2005; van den Bergh  
567 *et al.*, 2009; Roberts and Wooster, 2014; Hally *et al.*, 2016), and in some cases has been  
568 shown to detect fires unidentifiable using the more standard contextual approach (van  
569 den Bergh *et al.*, 2009; Roberts and Wooster, 2014).

570

571 **4.1.5 Non-thermal infrared methods**

572

573 AF detection methods using visible (VIS), NIR and SWIR band data have been  
574 developed for nighttime use. The VIS-NIR band (0.5 - 0.9  $\mu\text{m}$ ) on the 2.7-km U.S. Air  
575 Force DMSP-OLS sensor (Elvidge *et al.*, 1996) enabled nighttime detection of city lights,  
576 lightning flashes and active fires using a simple contextual algorithm that identified

577 pixels far brighter than its neighbors. Elvidge *et al.* (2013) extended the approach to 750  
578 m VIIRS day-night band (0.5 - 0.9  $\mu\text{m}$ ) data, combining it with that from the SWIR-to-  
579 LWIR bands and using a Planck function fitting approach to more confidently  
580 discriminate fires from other visible light sources. Some nighttime AF detection  
581 algorithms also employ SWIR radiances measures where available. For example, Elvidge  
582 *et al.* (2015) combined Landsat-8 SWIR and LWIR data to discriminate flaming and  
583 smoldering peatland fires, whilst Fisher and Wooster (2019) used nighttime SLSTR  
584 SWIR and MIR data to discriminate gas flares from vegetation fires.

585 Daytime SWIR algorithms have also been developed for use with medium spatial  
586 resolution sensors having no MIR capability. The most common approaches, developed  
587 for ASTER (Giglio *et al.*, 2008) and then Landsat-8 (e.g., Schroeder *et al.*, 2016, Kumar  
588 and Roy, 2018) rely on a fire-sensitive SWIR band and a comparatively insensitive NIR  
589 band to identify the increased SWIR radiance associated with fires (Figure 6).  
590 Commission errors can result from some highly reflective non-burning surfaces (e.g.,  
591 certain buildings), but the joint availability of Landsat-8 and Sentinel-2 imagery  
592 provides  $\sim$ 3-day median global coverage (Li and Roy, 2017) and the potential for  
593 relatively infrequent but spatially detailed global AF detection.

594 Finally, more experimental techniques requiring still novel sensors have been  
595 developed. For example, the identification of specific narrow-band NIR emission lines  
596 related to the thermal excitation of potassium (K) that occurs only in flaming fires has  
597 seen an early demonstration from space (Amici *et al.*, 2011).

598  
599

## 600 **5. Fire Radiative Power (FRP) and Fire Characterization**

601  
602 **5.1 FRP Retrieval**  
603

604 Since the late 1990's, AF detections have been increasingly accompanied by efforts at  
605 fire characterization, mostly in terms of retrievals of fire radiative power (FRP; usually  
606 expressed in MW). FRP is the rate at which the fires within a pixel are emitting thermal  
607 energy, integrated over all angles and wavelengths. An empirically-derived algorithm for  
608 direct estimation of FRP was first proposed and demonstrated with MODIS airborne

609 simulator data by Kaufman *et al.* (1998) - Equation [1]. An underlying assumption is  
 610 that, since heat yields are relatively constant among vegetation types (Stott, 2000),  
 611 remotely sensed FRP retrievals provide data useful for estimating rates of fuel  
 612 consumption and smoke emission, as first demonstrated by Wooster *et al.* (2005) and  
 613 Kaufman *et al.* (1998), Freeborn *et al.*, (2008) and Ichoku *et al.* (2008) respectively.  
 614 Equation [1] was used to retrieve FRP in the early (Collections 1 - 4) MODIS AF  
 615 Products (Giglio *et al.*, 2003), in units of emitted power per unit area of the pixel:  
 616

$$617 \quad FRP = 4.34 \times 10^{-19} \sum (T_{MIR,fire}^8 - T_{MIR,bg}^8) \quad [1]$$

619  
 620 where  $T_{MIR,fire}$  and  $T_{MIR,bg}$  are the MIR BT (K) of the AF pixel and the mean of the  
 621 surrounding “background” pixels respectively.

622 Whilst Equation [1] performs well for MODIS, its empirical nature means it is specific to  
 623 data from that sensor. It starts to underperform when applied to finer spatial resolution  
 624 data that record higher BTs due fires covering a greater proportion of their pixel area  
 625 (Section 3) (Wooster *et al.*, 2003). Wooster *et al.* (2003, 2005) derived a more  
 626 physically based approach to FRP retrieval, based on a power-law approximation to the  
 627 Planck function and which linearly related FRP (MW) to the AF pixels excess MIR  
 628 spectral radiance above the background:

$$630 \quad FRP = \frac{A_{sampler} \sigma \varepsilon}{\varepsilon_{MIR}} (L_{MIR,fire} - L_{MIR,bg}), \quad [2]$$

633  
 634 where  $\sigma$  is the Stefan-Boltzmann constant ( $5.67 \times 10^{-8} \text{ J s}^{-1} \text{ m}^{-2} \text{ K}^{-4}$ ) and  $\varepsilon$  and  $\varepsilon_{MIR}$  are the  
 635 broadband and MIR spectral emissivities respectively (that cancel as the fire is generally  
 636 considered a greybody or blackbody),  $L_{MIR}$  is the MIR spectral radiance of the AF pixel  
 637 ( $\text{W m}^{-2} \text{ sr}^{-1} \mu\text{m}^{-1}$ ), and  $L_{MIR,bg}$  is the estimate of what the AF pixel spectral radiance  
 638 would be if it did not have a fire within it (typically taken as the mean or median MIR

639 spectral radiance of the surrounding background pixels),  $\alpha$  (W m<sup>-2</sup> sr<sup>-1</sup>  $\mu$ m<sup>-1</sup> K<sup>-4</sup>) is a  
 640 coefficient dependent upon the sensor's MIR channel spectral response (Wooster *et al.*,  
 641 2005), and  $A_{sampler}$  is pixel area (km<sup>2</sup>).

642 Similar to its use in Equation [2], for MODIS Collection 5 an  $A_{sampler}$  multiplier  
 643 was added to Equation [1] to provide MODIS FRP outputs directly in MW, and from  
 644 Collection 6 onwards the FRP retrieval method was shifted to Equation [2] (Giglio *et al.*,  
 645 2016). Giglio *et al.* (2016) found an average 16% difference when comparing MODIS'  
 646 FRP retrievals based on Equations [1] and [2], with greater differences at lower FRPs  
 647 reflecting the fact that the MIR radiance method tends to underestimate FRP for  
 648 emitters < 600K (a lower temperature than that of most active combustion zones;  
 649 Wooster *et al.*, 2003; Dennison 2006). This underestimation is not necessarily  
 650 disadvantageous, since it means that radiant heat from warm, recently burned areas not  
 651 actively consuming fuel often do not contribute significantly to the total per-pixel FRP  
 652 measure from which combustion rates are often derived (Wooster *et al.*, 2005).  
 653 However, it may prove more problematic in peatland fires, where underground  
 654 combustion can lead to rather low surface temperatures in the burning areas (e.g.  
 655 Elvidge *et al.*, 2015; Fisher *et al.*, 2020).

656

657 Moving beyond the single-band FRP retrieval methods discussed above, another  
 658 approach to FRP estimation is to exploit outputs of the 'bi-spectral' method introduced  
 659 in Section 4.1.1, namely the effective fire temperature ( $T_f$ , K) and sub-pixel proportion  
 660 ( $p_f$ ) of the Matson (1981) and Matson and Dozier (1981) approach:

661

$$662 L_{MIR} = \tau_{MIR} p_f B_{MIR}(T_f) + (1 - p_f) L_{MIR,bg} \quad [3]$$

663

$$664 L_{LWIR} = \tau_{LWIR} B_{LWIR}(T_f) + (1 - p_f) L_{LWIR,bg} \quad [4]$$

665

$$666 FRP = \sigma(T_f^4 - T_{bg}^4) p_f A_f \quad [5]$$

667

668

669 where  $L_x$  is the AF pixel spectral radiance ( $\text{W m}^{-2} \text{ sr}^{-1} \mu\text{m}^{-1}$ ) observed in the denoted  
670 spectral band  $x$ ,  $B_x(T)$  is the Planck function ( $\text{W m}^{-2} \text{ sr}^{-1} \mu\text{m}^{-1}$ ),  $\tau$  is the atmospheric  
671 transmittance,  $L_{X,bg}$  is the ambient background spectral radiance (i.e. non-fire,  $\text{W m}^{-2} \text{ sr}^{-1} \mu\text{m}^{-1}$ ),  
672  $\sigma$  is the Stefan-Boltzmann constant ( $5.67 \times 10^{-8} \text{ J s}^{-1} \text{ m}^{-2} \text{ K}^{-4}$ ) and  $T_{X,bg}$  is the  
673 brightness temperature (K) of the ambient background in band  $x$ .

674

675 Per-pixel errors of  $T_f$  and  $p_f$  can be large, especially for lower values of  $p_f$ , and errors of  
676  $\sim 100$  K and  $\pm 50\%$  respectively at one standard deviation ( $\sigma_\eta$ ) were demonstrated for  
677 even easily detectable active fires ( $p_f > 0.005$ ; or 0.5% of the pixel area) by Giglio and  
678 Kendall (2001). This is mainly due to challenges in sufficiently precisely isolating the  
679 difference between the AF and ambient background pixel signals in the LWIR - where  
680 fire thermal emission is far less strong (Figures 5, 6 and 7), though errors in  $T_f$  and  
681  $p_f$  may counteract each other somewhat when delivering FRP through Equation 5  
682 (Wooster and Rothery, 1997). Inter-band spatial misregistration effects can also impact  
683 bi-spectral estimation of  $T_f$  and  $p_f$  (Shephard and Kennelly, 2003), though Briess *et al.*  
684 (2003) and Zhukov *et al.* (2006) tackled this by applying the approach at the fire cluster  
685 (rather than AF pixel) level. Overall, whilst the geostationary GOES WFABBA product  
686 (Prins *et al.*, 1998) applied this approach for FRP estimation, it is not particularly  
687 recommended for use with moderate to low spatial resolution data (Giglio and  
688 Schroeder, 2014; Giglio and Kendall, 2001). Most LEO and GEO AF products now base  
689 their per-pixel FRP retrievals on the MIR radiance method of Equation 2 (Wooster *et*  
690 *al.*, 2003; 2005). This includes those from VIIRS (Csiszar *et al.*, 2014), Meteosat  
691 (Wooster *et al.*, 2015), Himawari (Xu *et al.*, 2017), GOES (Xu *et al.*, 2010; 2021), SLSTR  
692 (Xu *et al.*, 2021) and MODIS (Giglio *et al.*, 2016).

693 In 2020, the Committee on Earth Observation Satellites (CEOS) Land Product  
694 Validation (LPV) Subgroup indicated that the current validation level of satellite FRP  
695 products is less advanced than for burned area, partly due to the ephemeral nature of  
696 active fires and the logistical and technical difficulties posed when trying to get  
697 independent, simultaneous FRP observations to match satellite estimates. However, by  
698 exploiting repeated observations occurring near the MODIS swath edge, Freeborn *et al.*  
699 (2014a) showed that variations in the exact sub-pixel placement of the fire contribute

700 per-pixel MODIS FRP uncertainties that are normally distributed with  $\sigma_\eta = 26.6\%$ , with  
701 simulations demonstrating that at the scale of fire clusters this reduces to less than  $\sim 5\%$   
702 for fires containing in excess of  $\sim 50$  MODIS AF pixels. Such size-dependent FRP  
703 uncertainties should be considered during any intercomparison and/or validation of  
704 satellite-based FRP data.

705

## 706 **5.2 Fire Radiative Energy (FRE) Estimation**

707

708 Fire radiative energy (FRE, MJ) is the temporal integral of FRP between two  
709 points in time ( $t_0$  and  $t_n$ ) (Wooster *et al.*, 2005), defined for discrete, evenly spaced,  
710 temporal sampling as:

711

$$712 \quad FRE = \sum_{t_0}^{t_n} FRP_t \Delta t \quad [6]$$

713

714 where  $FRP$  is the fire radiative power (MW) at time  $t$  and  $\Delta t$  is the time (secs) between  
715 FRP retrievals. In fire ecology, the term fire radiative energy [or flux] density ( $J\ m^{-2}$ ) is  
716 sometimes used (e.g. Kremens *et al.*, 2010; Sparks *et al.* 2017), but should be limited to  
717 situations where estimates of radiant energy release at a point are required.

718 FRE estimates are best achieved from GEO data, because high imaging  
719 frequencies provide the best temporal sampling (Freeborn *et al.*, 2009; Roberts and  
720 Wooster, 2008; Li *et al.*, 2018; Ellicott *et al.*, 2009; Roberts *et al.*, 2018a). However, the  
721 typically coarser pixel areas of GEO sensors mean they often fail to detect the lower FRP  
722 component of a region's fire regime, and a single GEO imager provides neither global  
723 coverage nor high-quality observations at very high latitudes (Figure 4). Numerous  
724 methods have attempted to estimate FRE from more infrequent LEO-derived FRP data,  
725 for example from the  $\sim$  four daily observations provided by MODIS that broadly sample  
726 the diurnal fire cycle (e.g. Boschetti and Roy, 2009; Freeborn *et al.*, 2011). The most  
727 widely applied method represents the FRP diurnal cycle using a modified Gaussian  
728 (perhaps informed by past GEO-FRP data), tailoring its characteristics via MODIS  
729 observations when available (Ellicott *et al.*, 2009, Vermote *et al.*, 2009; Andela *et al.*,  
730 2015; Yin *et al.*, 2019). To counteract effects coming from the relatively small number of

731 daily MODIS observations, and the fact fires are differently detected depending on their  
732 position in the MODIS swath which has a 16-day repeat cycle (Freeborn *et al.*, 2009),  
733 most LEO-derived FRE estimates are delivered at lower spatio-temporal resolutions  
734 (e.g., 0.25°; 8 days).

735

736

## 737 **6. Satellite Active Fire and FRP Products**

738

739 The number of routinely available GEO and LEO AF products has grown  
740 substantially over the last two decades (Table 1), with several LEO products having  
741 global and/or multi-decade coverage (Arino *et al.*, 2012; Csiszar *et al.*, 2014; Giglio *et*  
742 *al.*, 2016; Xu *et al.*, 2020). Most use contextual AF detection methods (Section 4.1.3),  
743 with the NASA MODIS AF products demonstrating an excellent approach where re-  
744 processed Collections are periodically released based on algorithm refinements and  
745 updated calibration/geolocation information (Giglio *et al.*, 2003; 2016). Such updates  
746 are mostly driven by routine product quality and validation assessments, along with  
747 science developments (Justice *et al.*, 2002a; 2002b).

748 Assessing the absolute accuracy and precision of AF products is difficult for  
749 reasons discussed in Section 5. In addition to daytime sunglints, non-burning hot areas  
750 and regions of high local thermal contrast can result in AF detection errors of  
751 commission in places such as deserts, urban areas, and forest clear cuts (e.g. Schroeder  
752 *et al.* 2008; Kumar and Roy, 2018). Such effects are potentially magnified in higher  
753 spatial resolution products (e.g. Schroeder *et al.*, 2014; Zhang *et al.*, 2017). AF detection  
754 errors of omission are generally related to surface obscuration by cloud (or thick smoke  
755 removed incorrectly during cloud masking), fires not burning at the observation time, or  
756 small and/or too cool fires having an FRP below the products minimum detection limit  
757 (Giglio 2007; Roy *et al.*, 2008; Roberts *et al.*, 2015; Hall *et al.*, 2019). Commission  
758 errors for the best performing products range from a few percent to about 10%,  
759 depending on sensor and algorithm specifics. Some of the most mature (e.g., the NASA  
760 MODIS products) claim mean global commission errors of around 3% (Giglio *et al.*,  
761 2016). Mature geostationary AF products typically have similar commission errors to  
762 LEO products, but higher omission errors due to their larger area pixels and thus higher

763 minimum FRP detection limit (as is apparent in **Figures 5** and **8**). Conversely, the  
764 higher temporal frequency GEO AF products can sometimes identify fires that are not  
765 detected by LEO products, such as those ignited and burned out between LEO  
766 overpasses or in cloudy regions where the land surface is viewed briefly by the GEO data  
767 as the clouds move (Roberts and Wooster, 2008; Roberts *et al.*, 2015; Hally *et al.*, 2017).

768

769 **Table 1.** LEO and geostationary orbit systems used to generate Active Fire (and for  
770 some also FRP) products.

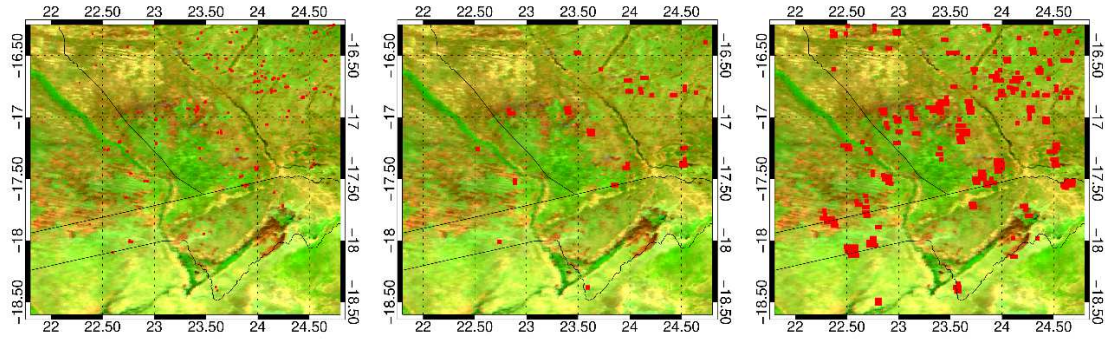
771

Instrument	Spatial resolution of active fire data	Geographic coverage	Satellite Orbit	Satellite / Agency
MODIS	1 km	Global	LEO	Terra, Aqua/ NASA
GOES ABI	2 km	75.2 ° W: North and South America 135 ° W: Pacific Ocean, Hawaii, North and South America	Geostationary	GOES-E and -W /NOAA
Himawari AHI	2 km	140.7 ° E: East Asia, Australia, Pacific Ocean	Geostationary	Advanced Himawari Imager (AHI), JAXA and JMA
Meteosat SEVIRI	3 km	0 °: Europe, Africa, 41.5 E	Geostationary	Eumetsat
VIIRS	375 m, 750 m	Global	LEO	S-NPP, JPSS1/NOAA 20 NASA/NOAA
NOAA AVHRR	1 km	Global	LEO	POES / NOAA METOP / Eumetsat

(A)ATSR	1 km	Global (but only nighttime AF product)	LEO	ERS-2* and ENVISAT
SLSTR	1 km	Global	LEO	Sentinel-3/ Eumetsat and ESA
HSRS	350 m	Global (but on-demand products)	LEO	Firebird Constellation / DLR

772

773 \*ERS-1 also carried an ATSR sensor, but its MIR channel failed soon after launch.



774

775

776

777 **Figure 8.** Active fire detections made on 31<sup>st</sup> August 2017 (red) in a region of southern  
778 Africa using (a) Terra MODIS and Aqua MODIS, (b) Meteosat SEVIRI observations  
779 made near-simultaneously with MODIS, and (c) all SEVIRI data collected over that day  
780 (24-hrs). Background is a MODIS surface reflectance image (RGB: 2.1  $\mu$ m, 0.8  $\mu$ m and  
781 0.6  $\mu$ m).

782

## 783 7. AF Relationships to Fuel Consumption and Atmospheric Variables

784

### 785 7.1 Fuel Consumption Estimation

786

787 One of the earliest applications of satellite data related to landscape fires was to  
788 estimate amounts of dry biomass consumed ( $M_{consumed}$ ) (Seiler and Crutzen, 1980). The  
789 standard methodology is to combine satellite-derived burned area (BA) data with  
790 biome- and date-dependent fuel consumption per unit area ( $F_c$ ) estimates, and this is  
791 the basis of the widely-used Global Fire Emission Database (GFED, van der Werf *et al.*,  
792 2017). However, the method is unable to operate close to real time since BA data are  
793 typically only available after the fire event, and the  $F_c$  estimates rely on environmental  
794 models driven by meteorological and other data only available with a time delay. As  
795 detailed in Section 5 however, FRP measures can provide almost real-time information  
796 directly proportional to rates of fuel consumption and smoke emission. FRE (MJ)  
797 estimates derived from laboratory-scale 1 Hz FRP measures of mainly cured dry grass  
798 fires were shown to be linked to dry biomass consumed via an ‘FRE combustion  
799 coefficient’ ( $F_c$ ) of  $0.37 \pm 0.02 \text{ kg MJ}^{-1}$  (Wooster *et al.*, 2005):

800

$$801 M_{consumed} (\text{kg}) = 0.37 \times FRE (\text{MJ}) \quad [7]$$

802

803 Confirmation of similar ‘combustion coefficient’ values for other fuels was  
804 subsequently demonstrated in further small-scale fire experiments (e.g. Freeborn *et al.*,  
805 2008; Kremens *et al.*, 2012), and the FRE approach to fuel consumption estimation  
806 been applied to landscape-scale fires using EO data from e.g. Meteosat SEVIRI (Roberts  
807 *et al.* 2005; 2011; 2018a), GOES (Li *et al.*, 2018) and MODIS (Ellicott *et al.*, 2009;  
808 Vermote *et al.*, 2009; Kaiser *et al.*, 2012; Andela *et al.*, 2015; Yin *et al.*, 2019; McCarley  
809 *et al.*, 2020). However, spaceborne FRP retrievals are subject to perturbations beyond  
810 those affecting small-scale field or laboratory studies, potentially altering the effective  
811 value of the FRE combustion coefficient. Mota and Wooster (2018) summarize such  
812 effects as coming from AF omission errors (Section 4.2), interception of surface-emitted  
813 radiation by overlying tree canopies (Roberts *et al.*, 2018b, Mathews *et al.*, 2016;  
814 Johnston *et al.*, 2018), atmospheric effects (Wooster *et al.*, 2015), fuel moisture  
815 variations (Smith *et al.*, 2013), and potentially fire size-dependent variations in the  
816 radiative fraction of the fuel heat yield (Freeborn *et al.*, 2008). Such effects may be  
817 responsible for the generally larger and biome-dependent FRE combustion coefficients

818 derived by Kaiser *et al.* (2012) derived from Global Fire Assimilation System (GFAS)-  
819 based FRE estimates and GFED (burned area)-based fuel consumption totals. Despite  
820 remaining uncertainties, the FRP and FRE approach provides the only direct route to,  
821 respectively, rapidly estimating fuel consumption and smoke emission rates whilst a fire  
822 is burning, and the totals of these immediately after a fire has ceased. Further benefits  
823 may stem from removing the use of models that are sometimes difficult to parameterize,  
824 for example Nguyen and Wooster (2020) demonstrated one of the first EO-based  
825 mappings of fuel consumption per unit ( $F_c$ ) area across Africa, based solely on Meteosat  
826 FRE data and 20 m spatial resolution BA mapping.

827

828 **7.2 Smoke Emissions Estimation from Active Fire Data**

829

830 Fire emissions estimation is one of the main applications for EO-derived data on  
831 active fires. Johnston *et al.* (2012) used GFED data and a global atmospheric model to  
832 estimate that hundreds of thousands of excess deaths annually are related to exposure to  
833 smoke from landscape fires, and Roberts and Wooster (2021) recently revised this  
834 estimate upwards based on the FRP-based smoke emissions estimates provided by  
835 GFAS. Emissions of a particular smoke species are typically estimated using:

836

837 
$$M_x = EF_x \times M_{consumed} \quad [8]$$

838

839 where  $M_x$  is the mass of the emitted species  $x$  (g) and  $EF_x$  its emission factor ( $\text{g} \cdot \text{kg}^{-1}$ ).

840

841 However, in part due uncertainties in the ‘combustion coefficient’ values of Equation 7  
842 associated with different satellite datasets and/or biomes (see Section 6.1) there is an  
843 interest in relating spaceborne FRP estimates directly to rates of smoke emission ( $R_x$ ),  
844 first demonstrated by Ichoku and Kaufman (2005):

845

846 
$$R_x = C_e^x \times FRP \quad [9]$$

847

848 where,  $R_x$  is the rate of emission of species  $x$  (expressed in  $\text{kg.s}^{-1}$ ) and  $C_e^x$  is the emission  
 849 coefficient for species  $x$  ( $\text{kg.MJ}^{-1}$ ).

850

851 Values of  $C_e^x$  are typically derived from comparisons between satellite-derived  
 852 FRP datasets and the emitted species in question, primarily at present particulate  
 853 matter (PM) amounts estimated via aerosol optical depth (AOD) measures (Ichoku and  
 854 Kaufman, 2005; Mota and Wooster, 2018; Nguyen and Wooster, 2020). The approach  
 855 has been successfully demonstrated for near real-time PM emissions estimation in the  
 856 U.S. (e.g. Jordan *et al.*, 2008), Canada (e.g. Henderson *et al.*, 2008), and Europe (e.g.  
 857 Sofiev *et al.*, 2009), and for global-to-continental scale emissions estimation to support  
 858 science studies (e.g. Vermote *et al.*, 2009; Ichoku and Ellison, 2014; Mota and Wooster,  
 859 2018; Nguyen and Wooster, 2020). Table 3 lists the major global fire emissions datasets  
 860 derived from satellite AF datasets, including GFED since whilst it primarily uses burned  
 861 area data it uses AF detections to aid BA estimation in certain circumstances (see  
 862 Section 8).

863

864 Table 3: Global fire emissions inventories and real-time monitoring systems based in  
 865 part on satellite AF data. Note that those not updated in near real time are less  
 866 appropriate for use in e.g. atmospheric monitoring and forecasting systems. Note  
 867 that FREMv2 is based on FRP measures derived from GEO systems and so is not  
 868 global. We focus on here on that derived from Meteosat over Africa.

869

<b><i>Emission Dataset Name, and version, and access*</i></b>	<b><i>Spatial Resolu- tion</i></b>	<b><i>Highest Tempo- ral Freque- ncy</i></b>	<b><i>Satellite Active Fire Obs Used<sup>#</sup></i></b>	<b><i>Emissio- n Factor / Coeffici- ent</i></b>	<b><i>Data Availabil- ity period</i></b>	<b><i>Example Reference<sup>@</sup></i></b>
FINN_v1.5	1 km	Daily	$N_{pix}$	$EF_x$	2002– Present	Wiedinmyer <i>et al.</i> , 2011
FLAMBE- ARCTAS	1-4 km	Hourly	$N_{pix}$	$EF_x$	2000– Present	Reid <i>et al.</i> , 2009

GBBEPx_v2	0.25 deg	Daily	FRP	$EF_x$	2017–Present	<i>Zhang et al., 2012</i> <i>Zhang et al., 2017</i>
GFAS_v1.2	0.1 deg	Daily	FRP	$EF_x$	2001–Present	<i>Kaiser et al., 2017</i>
GFED_v3.1	0.5 deg	3-hourly	BA, $N_{pix}$	$EF_x$	1997–2011	<i>van der Werf et al., 2010</i>
GFED_v4.1s	0.25 deg	3-hourly	BA, $N_{pix}$	$EF_x$	1995–Present	<i>van der Werf et al., 2017</i>
FEER_v1.0-G1.2	0.1 deg	Daily	FRP	$C_e^x$	2003–Present	<i>Ichoku and Ellison, 2014</i>
IS4Fires_v2.0	0.1 deg	3-hourly	FRP	$C_e^x$	2000–Present	<i>Sofiev et al., 2009</i>
QFED_v2.5	0.1 deg	Daily	FRP	$C_e^x$	2000–Present	<i>Darmenov and da Silva, 2015</i>
FREMV2	Per-Pixel & 0.1 deg	15 mins	FRP	$C_e^x$	2004–Present	<i>Nguyen and Wooster, 2020</i>

\*Dataset websites as of March 2021:

FINN (<https://www2.acom.ucar.edu/modeling/finn-fire-inventory-ncar>);

FLAMBE (not available);

GFAS (<https://www.ecmwf.int/en/forecasts/dataset/global-fire-assimilation-system>);

GFED (<http://www.globalfiredata.org/>);

FEER (<https://feer.gsfc.nasa.gov/data/emissions/>);

IS4Fires (<http://is4fires.fmi.fi>);

QFED ([http://wiki.seas.harvard.edu/geos-chem/index.php/QFED\\_biomass\\_burning\\_emissions](http://wiki.seas.harvard.edu/geos-chem/index.php/QFED_biomass_burning_emissions));

GBBEP (<http://www.ospo.noaa.gov/Products/land/gbbepx/>)

#This includes the parameter type used in generating the emission dataset (and the sensor/satellite that acquired such observations enclosed in parenthesis):  $N_{pix}$ =fire-pixel count; FRP=fire radiative power

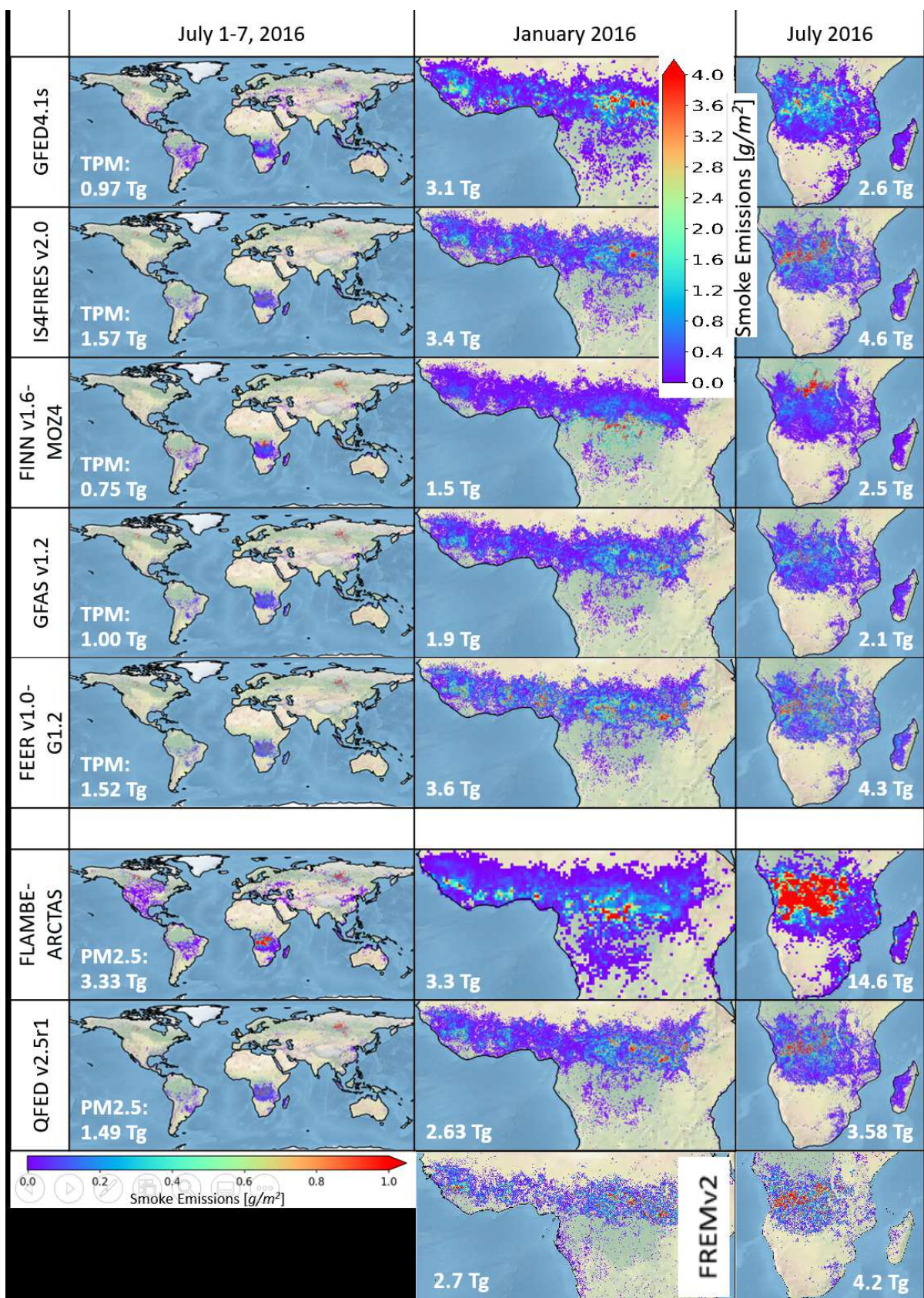
884 @The indicated references are respective representative examples but may not be the  
885 most relevant reference for each dataset.

886

887 **Figure 9** shows an emissions inventory intercomparison for seven of the datasets  
888 detailed in Table 3 (1-7 July 2016) available globally, both worldwide and for the peak  
889 fire month in northern and southern hemisphere Africa. Although it would have been  
890 best to show the same smoke aerosol species (in this case, total particulate matter; TPM)  
891 for all products, FLAMBE and QFED only provide PM<sub>2.5</sub> so this is shown instead.  
892 Continued uncertainty in fire emissions estimates is evidenced by the more than two  
893 times difference among the TPM emissions estimates, and the larger differences when  
894 considering PM<sub>2.5</sub>. Other estimates, conducted as yet only for Africa, show similar  
895 ranges of estimation (Nguyen and Wooster, 2020). Nevertheless, there appears to be  
896 some improvement compared to the factor of 12 difference found even relatively  
897 recently (Zhang *et al.*, 2014). Uncertainties stem from a combination of and/or  
898 propagation of errors that, depending on the exact method and calculations employed,  
899 come from the satellite-derived variables (e.g. AF pixel counts, FRP, and AOD), the  
900 aforementioned ‘combustion coefficient’ conversion factor, the representativeness of the  
901 emission factors (EF<sub>x</sub>), any required smoke injection height and velocity estimates, and  
902 the host of applicable model parameterizations/assumptions. Further research is  
903 needed to quantify the absolute magnitudes and sources of these uncertainties, and thus  
904 improve our current quantification of continental-to-global fire emissions.

905

906



908 **Figure 9:** Landscape fire emissions estimates of total particulate matter (TPM) or  
909 particulate matter of  $2.5 \mu\text{m}$  or less aerodynamic diameter ( $\text{PM}_{2.5}$ ), as contained within  
910 different fire emissions databases (Table 3). Left column: July 1-7, 2016 global  
911 distribution; Middle column: January 2016 northern sub-Saharan Africa distribution;  
912 Right column: July 2016 southern sub-Saharan Africa distribution. Total emission of  
913 the respective smoke species for the respective time periods is indicated on each panel.  
914 FREMv2 is based on geostationary data and so is not global.

915  
916

## 917 **8. Relationships to Fire Regimes and Ecosystem Variables**

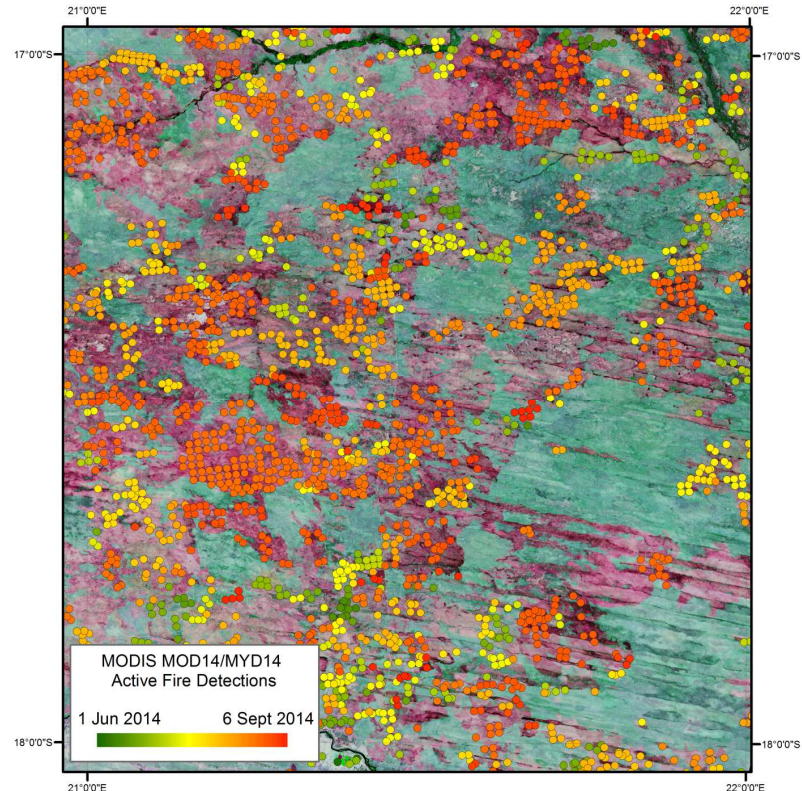
918 AF detections and FRP data are most commonly used to identify fire timing,  
919 location, intensity, and smoke emissions source strength. However, they have also been  
920 used to infer burned area, fire behavior and fire impacts on the terrestrial environment,  
921 both during and after fire events, and to help define areas characterized by different fire  
922 regimes.

923  
924

### **8.1 Burned Area**

925 Satellite data have been used for nearly 40 years to directly map burned area via a fires  
926 impact on surface reflectance (Chuveico *et al.*, 2019). However, in the 1980's and 1990's  
927 BA estimates were often calculated using AVHRR-derived AF pixel counts (e.g. Matson  
928 *et al.* 1987; Matson and Holben 1987) – mainly because AVHRR data are sub-optimal  
929 for direct BA mapping (Giglio and Roy, 2020). However, AF errors of omission related  
930 to e.g. cloud cover or to fires that were not burning at the satellite observation time  
931 mean that AF pixel counts often provide an imperfect proxy for area burned. **Figure 10**  
932 shows an area of burned savanna imaged by 30 m Landsat data and overlaid with  
933 contemporaneous MODIS AF detections. The latter document the spread of the fire but  
934 contain extensive spatial gaps, and even interpolation of the AF detections would not  
935 fully reconstruct the full BA extent.

936



937  
938  
939

940 **Figure 10:** MODIS 1 km active fire pixel detections (shown with a rainbow color scale  
941 indicating the day of detection over a three month period) superimposed on a Landsat 8  
942 OLI image (R: 2.2  $\mu$ m, G: 0.86  $\mu$ m, B: 1.6  $\mu$ m, burned areas are apparent in magenta  
943 tones) acquired on the last day of the MODIS active fire detections (6<sup>th</sup>  
944 September, 2014) for 100 km  $\times$  100 km over the Caprivi Strip on the border between  
945 Angola and Namibia.

946  
947 Whilst **Figure 10** shows a clear pattern between BA extent and matching AF pixel  
948 count, several studies (e.g. Giglio *et al.*, 2013; Hantson *et al.*, 2013) demonstrate the  
949 ratio to be biome-dependent. These include Roy *et al.* (2008) who found that for low  
950 percent tree cover and leaf area index (LAI) landscapes, the MODIS 500 m BA product  
951 defined a greater proportion of the landscape as burned than did the MODIS AF  
952 product; yet with increasing tree cover (>60%) and LAI (>5) the reverse was often true.  
953 Biome-specific calibrations have been undertaken to estimate BA from AF pixel counts

954 (Scholes *et al.*, 1996; Giglio *et al.*, 2013), with for example GFED using nighttime ATSR  
955 AF detections (Arino *et al.*, 1999) to estimate BA for the pre-MODIS 1997-2000 period  
956 via:

957

958  $BA_{i,t} = \alpha_i AF_{i,t}^{\beta_i}$  [12]

959

960 where  $BA_{i,t}$  is the burned area in grid cell  $i$  and month  $t$  ( $0.25^\circ$  grid cells),  $AF_{i,t}$  is the AF  
961 detection for the same cell and time, and  $\alpha_i$  and  $\beta_i$  are dimensionless and spatially-  
962 varying parameters estimated independently using regression of post-2000 ATSR AF  
963 pixel counts (Arino *et al.*, 1999) with the 500 m MODIS BA product (Giglio *et al.* 2013).

964

965 Some of the most recent iterations of GFED (e.g. v4.1s; van der Werf *et al.*, 2017) also  
966 use satellite AF detections to estimate the additional BA associated with fires too small  
967 to be mapped with the MODIS 500 m BA product. Whilst this ‘small fire boost’  
968 successfully increases BA in many regions, it can also lead to significant errors in  
969 locations subject to many AF detection errors of commission (Zhang *et al.*, 2018). This  
970 points to the importance of understanding the regional and seasonal dependencies of AF  
971 detection errors.

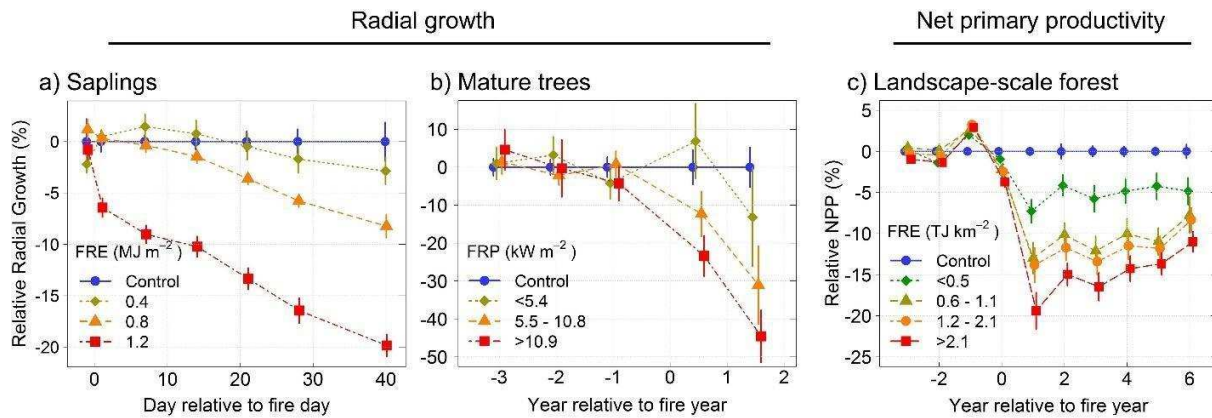
972

## 973 **8.2 Rate of Spread and Intensity and Relationships to Fire Effects**

974 Some of the most ecologically important characteristics of an actively spreading  
975 landscape fire are the fire front rate of spread (ROS) and fireline intensity (FLI; Byram,  
976 1959) (Bond and Keeley, 2005). AF data have been related to both – though primarily  
977 those based on airborne rather than satellite observations (e.g. Pastor *et al.*, 2006;  
978 Paugam *et al.*, 2013). Most satellite AF data use has been limited to mapping wildfire  
979 progression across the landscape (e.g. Veraverbeke and Hook, 2013), and whilst ROS  
980 estimation has been attempted from LEO (Andela *et al.*, 2019) and occasionally GEO  
981 (Liu *et al.*, 2020) AF data, the low spatial and/or temporal resolution of the source data  
982 provides limitations. FLI represents the rate of heat release per unit time per unit length  
983 of the fire front ( $\text{kW m}^{-1}$ ; Alexander, 1982), and unlike FRP it includes the all heat  
984 transfer mechanisms. Thus any FRP-based FLI calculations need to assume a radiant

fraction, or simply provide the FLI radiative component only (e.g. Wooster *et al.*, 2004; Riggan *et al.*, 2004; Smith and Wooster, 2005). FRP-derived values of fire heat release may provide links to the effects on plant physiology, such as pre-and post-fire change in net photosynthesis, tree radial growth, or landscape-scale forest net primary production (NPP) change (e.g. Sparks *et al.*, 2017; 2018; **Figure 11**).

990



991

992

993 **Figure 11.** Radial tree growth and NPP patterns seen across different temporal and  
994 spatial scales in areas subject to varying levels of fire activity (as expressed by FRP and  
995 FRE per unit area values at (a) 2 yr old *Pinus contorta* saplings in laboratory  
996 experiments and (b) mature (>35 years old) *Pinus ponderosa* trees burned in stand-  
997 scale prescribed fires respectively. Similar patterns were observed in (c) at the regional  
998 scale using net FRE per unit area and NPP measures derived from MODIS. See Sparks  
999 *et al.* (2017; 2018).

1000

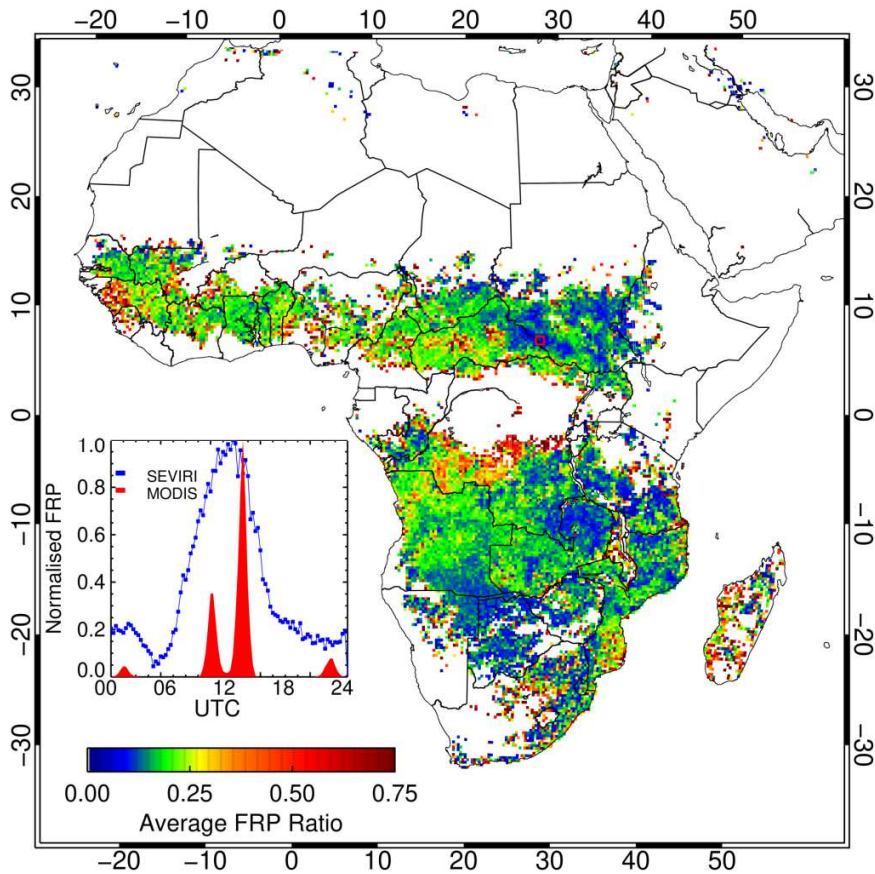
### 1001 **8.3. Fire regime characterization**

1002

1003 A fire regime describes the prevailing, long-term fire patterns and characteristics  
1004 of an area, emerging from feedback interactions between climate, vegetation, and the  
1005 regions natural and anthropogenically driven fires (Whitlock *et al.*, 2010). A fire regimes  
1006 principle characteristics are fire *frequency*, *seasonality*, *spread patterns*, *intensity* and  
1007 *fuel consumption* (Bond and Keeley 2005; Gill 1975). Satellite AF data have been used to  
1008 provide contemporary views of landscape fire regimes and to distinguish parameters

related to fire size, intensity, severity, and most commonly fire seasonality, frequency and diurnal cycle. Each LEO sensor such as AVHRR, MODIS, and VIIRS typically image areas a few times daily per satellite, enabling fire diurnal cycles to be roughly characterized using either day/night ratios (Giglio *et al.* 2006; Langaas 1992) or interpolation between observations (Andela *et al.* 2015; Ellicott *et al.* 2009). The TRMM low-inclination, drifting orbit enabled fire diurnal cycles to be characterized from 8-yrs of VIRS data (Giglio 2007), but the high temporal resolution (and constant ground footprint areas) provided by geostationary sensors are optimum for diurnal cycle characterization. GEO data have been applied for this purpose across the Americas (e.g. Prins *et al.*, 1998; Xu *et al.*, 2010; Zhang *et al.*, 2012), east and south-east Asia (e.g. Hyer *et al.*, 2013; Xu *et al.*, 2017) and Africa (e.g. Roberts *et al.*, 2009; 2018a) (**Figure 12**).

1021



1022

1023 **Figure 12.** Fire radiative power (FRP) diurnal cycle variability across Africa, as derived  
1024 from a year of the 96 daily FRP datasets provided by the geostationary Meteosat FRP-  
1025 PIXEL product available from the EUMETSAT LSA-SAF (Wooster *et al.*, 2015; Roberts  
1026 *et al.*, 2015). Generally, the fire diurnal cycle is semi-Gaussian, with a day-time peak and  
1027 nighttime minima (see inset that shows normalized FRP values from SEVIRI and  
1028 MODIS), but the timing of the peak spatially varies. The metric shown is the ratio  
1029 between the summed FRP measured by SEVIRI at only the times of MODIS overpasses,  
1030 and that measured over the full 24-hr cycle. Changes in the timing of the diurnal cycle  
1031 peak are reflected in changes to this ratio.

1032  
1033 Satellite AF data indicate that fire diurnal cycles are mostly characterized by mid-  
1034 afternoon (local solar time) peaks, with less activity (and with generally lower  
1035 intensities) between late evening and early morning (Giglio, 2007; Hyer *et al.*, 2013;  
1036 Roberts *et al.*, 2009). During droughts, increased combustion of deep organic soils  
1037 sometimes results in a less pronounced and/or temporally extended diurnal cycle (e.g.  
1038 Kaiser *et al.*, 2012; Wooster *et al.*, 2012a; 2018), whereas in agricultural regions a bi-  
1039 modal diurnal cycle may be driven by local burning practices (Xu *et al.*, 2017). New fire  
1040 seasons can also sometimes rapidly arise, driven by changes in fire policy and/or  
1041 enforcement (e.g. Zhang *et al.*, 2020). Further fire regime characteristics derivable from  
1042 satellite AF data include size distributions, sometimes derived from FRP (e.g. Wooster  
1043 and Zhang, 2004) though more commonly from BA (e.g. Archibald *et al.*, 2010). Fire  
1044 type can sometimes be elucidated, with clusters of adjacent AF pixels deployed to  
1045 identify spatially contiguous flaming and smoldering areas (Langaas, 1992), and on an  
1046 instantaneous basis large AF pixel clusters can either be associated with long and  
1047 narrow fire lines such as found in savannas (e.g. Dwyer *et al.*, 2000), or deep flaming  
1048 fronts with residual combustion behind, typical of Canadian forest fires (Cahoon *et al.*,  
1049 2000). Fire regimes in areas with higher fuel loads and which burn under hotter, drier,  
1050 and windier conditions generally exhibit higher upper limits of FLI ( $\text{W.m}^{-1}$ ), reaction  
1051 intensity ( $\text{W.m}^{-2}$ ), and heat release per unit area ( $\text{J.m}^{-2}$ ). These are key fire behavior  
1052 attributes influencing fires' short- and long-term ecological impact, though thus far their  
1053 estimation is only rarely attempted from AF data (see Section 7). More commonly, FRE-

1054 derived fuel consumption totals (Section 7) have been ratioed against BA data to derive  
1055 fuel consumption per unit area measures (e.g. Roberts *et al.*, 2011; Mota and Wooster,  
1056 2018; Nguyen and Wooster, 2020), and have been used to help discriminate identical  
1057 fire regimes happening at different times of the year under variable meteorological  
1058 conditions (e.g., Andela *et al.*, 2015; Boschetti and Roy 2009; Freeborn *et al.*, 2016).  
1059 FRP distributions themselves have revealed regional as well as intra-biome fire regime  
1060 variations (Wooster and Zhang 2004; Ichoku *et al.*, 2008; Giglio *et al.*, 2006; Laurent *et*  
1061 *al.*, 2019), though such differences may be due to variations in an unknown combination  
1062 of fire behavior attributes (e.g. radiant fraction, sub-pixel active fire area, fire intensity)  
1063 coupled with influences such as canopy overstory effects (Roberts *et al.*, 2018b).

1064 AF products are particularly well suited for characterizing fire seasons, or the  
1065 times of the year when large and intense fires are most prevalent. A variety of temporal  
1066 metrics (e.g., start and end dates, peak month, and fire season duration etc.) have been  
1067 derived from both AF pixel counts and FRP data, and used to map regional to global  
1068 variations in fire seasonality (e.g. Dwyer *et al.*, 2000; Giglio *et al.*, 2006). Locations  
1069 where the fire season leads or lags seasonal weather may indicate the degree of control  
1070 that humans exert on a regions fire regime (Le Page *et al.*, 2010). For example, across  
1071 much of northern Africa, rural communities purposely ignite early season fires under  
1072 mild weather conditions to create a patchwork of fuel breaks in an attempt to limit the  
1073 uncontrolled spread of more intense and more ecologically damaging late season fires  
1074 (Laris, 2002). Agricultural residue burning periods similarly closely coincide with the  
1075 timing of crop-specific planting and harvesting (Korontzi *et al.*, 2006; McCarty *et al.*,  
1076 2009; Zhang *et al.*, 2018; 2020)

1077 Accumulating many years of AF observations allows retrieval of long-term attributes,  
1078 such as fire return interval (average number of years between successive fires), fire  
1079 frequency (the inverse of fire return interval), and measures of interannual fire  
1080 variability and trend. However, derived chronologies of annual fire occurrence have  
1081 been more commonly extracted from BA time-series (Devineau *et al.*, 2010; Freeborn *et*  
1082 *al.*, 2014b). Instead, the simplest and most common AF analog has probably been the  
1083 count of AF pixels detected per unit time and per unit area, referred to as both fire  
1084 frequency and fire density (Chuvieco *et al.*, 2008; Csizsar *et al.*, 2005; Di Bella *et al.*,  
1085 2006; Soja *et al.*, 2004). Temporal trends in AF pixel counts are most often used to infer

1086 changes in fire occurrence and when associated with time-series of climate, land cover,  
1087 and anthropogenic variables have been used to identify locations of shifting fire regimes  
1088 potentially associated with anthropogenic or climatic trends (Aragao and Shimabukuro,  
1089 2010; Arino *et al.* 2012; Gregoire and Simonetti, 2010; Pricope and Binford, 2012).

1090

## 1091 **9. Online AF Data Delivery and Mapping Systems**

1092

1093 Whilst certain of the AF products outlined in Section 6 have been available for  
1094 several decades, widespread product delivery in easily accessible formats has been  
1095 available for only around half this time. The MODIS Rapid Response System was the  
1096 first attempt to provide near real-time global AF data (Justice *et al.*, 2002a),  
1097 subsequently evolving into the NASA Fire Information for Resource Management  
1098 System (FIRMS) (Davies *et al.*, 2014). These developments are part of a growing trend  
1099 of “analysis ready data” (ARD), which aims to reduce the EO data pre-processing burden  
1100 on users and enable easier and more immediate analyses. AF data are made available  
1101 typically with very low data latency rates via these and other systems, generally within a  
1102 few hours or less of the observation time.

1103 AF detections have been available in analysis ready form for more than two decades,  
1104 and this has helped spread their use in multiple applications. Many of these need not  
1105 expose the user to detailed knowledge of the methods and algorithms (outlined in  
1106 earlier Sections) that have been used to produce the AF data. Applications include  
1107 strategic land and fire management, no-burning compliance monitoring, wildlife  
1108 conservation, detection of illegal logging and/or poaching within protected areas,  
1109 monitoring air pollution and improved understanding of fire regimes. As applications  
1110 for AF data have evolved and matured, users have further articulated their information  
1111 requirements (e.g., Trigg and Roy, 2007; Mouillot *et al.* 2014; Davies *et al.*, 2014), which  
1112 in turn has led to more customized data products, more functional and accessible online  
1113 data mapping and delivery systems including a wider variety of variables, and most  
1114 recently also mobile accessible applications. Whilst some users simply wish to visualize  
1115 AF data on a map, and others want to download it for their own analyses, increasingly  
1116 there is a move to also provide broader contextual information in a single online  
1117 application (e.g. land cover; atmospheric composition; fire risk, BA).

1118 AF fire data delivery systems can be classified into three groups: 1) direct providers,  
1119 who process and distribute their own AF data; 2) brokers, who take AF data from a  
1120 direct provider and add value by customizing the information to serve specific user  
1121 communities; and 3) those that are both direct providers and brokers. The latter often  
1122 process data collected ‘locally’ in real-time via a so-called satellite direct reception (DR)  
1123 or direct broadcast (DB) station, but also acquire additional AF data from others to  
1124 provide broader geographic coverage. AF data users are now faced with a huge choice of  
1125 data portals, and Appendix 2 provides detail on four key examples currently operating.  
1126 We also include therein an example of how such data are used, in this case in support of  
1127 national park fire management. Users select their most appropriate information delivery  
1128 system based on data type and coverage, latency (time from satellite overpass to user  
1129 availability), ease of use, and how the AF data can be viewed and queried alongside  
1130 other types of information. GEO or DR-based LEO data feeds generally have some of the  
1131 lowest data latency times, but more recently even non-DR equipped data portals for  
1132 MODIS and VIIRS AF data, such as NASA FIRMS (part of NASA’s Land, Atmosphere  
1133 Near real-time Capability for EOS (LANCE)) offer AF data updates usually within 2.5  
1134 hours of the observation time, though some specifics of the near real-time (NRT) AF  
1135 products served may differ from those of the “standard” data products. New data feeds  
1136 are following this trend, with AF detections and FRP data Sentinel-3 (Wooster *et al.*,  
1137 2012b; Xu *et al.*, 2020) produced in two versions, NRT within a few hours of data  
1138 capture (<https://metis.eumetsat.int/frp/>), and non-time critical (NTC) a few days later  
1139 (<https://scihub.copernicus.eu/dhus/#/home>) .  
1140

## 1141 **10. Future Priorities in Active Fire Remote Sensing**

### 1142 **10.1 Dataset Priorities**

1144 NRT and higher spatial and temporal resolution satellite AF and FRP products  
1145 are a priority for the applications and science communities. Errors of AF commission  
1146 and in particular omission should continue to be reduced, through sensor and algorithm  
1147 development, robust validation, and provision of improved ancillary datasets such as  
1148 masks optimized for the AF-application, e.g. cloud masks which do not mask out smoke  
1149 contaminated areas, appropriate land/water maps, and maps of static IR emitters (e.g.

1150 gas flares/volcanoes and potentially persistent false alarms due to e.g. specific industry  
1151 or building types). Such developments are required to meet the temporal (1-6 hours)  
1152 and spatial (0.25-3 km) resolution and FRP retrieval uncertainty (10% integrated over a  
1153 pixel) target specifications outlined by the Global Climate Observing System (GCOS)  
1154 Essential Climate Variable (ECV) programme (GCOS-200; 2016) and proposed by  
1155 GOFC/GOLD and the Committee on EO Satellites (CEOS) Land Product Validation  
1156 (LPV) working groups (Boschetti *et al.*, 2009). The need for long-term, climate quality,  
1157 AF products offering global coverage remains paramount, and this entails systematic  
1158 product generation, quality control, algorithm maintenance and when necessary  
1159 reprocessing. Without reprocessing using updated calibration and geolocation  
1160 information, and improved algorithms refined in response to routine product quality  
1161 assessment periodic validations (Section 6), AF products become less suitable for  
1162 addressing climate science questions.

1163 In addition to improving AF detection algorithms, efforts should focus on  
1164 developing AF products maximizing use of currently available data, such as through  
1165 blending GEO and LEO observations (e.g. Zhang *et al.*, 2020). A long-standing  
1166 GOFC/GOLD goal is the development of a global geostationary AF system, which is  
1167 increasingly relevant given the improved AF fire detection apability of the new  
1168 generation of GEO satellites. AF detection and FRP data have recently become available  
1169 in NRT from Meteosat, Meteosat Indian Ocean, Himawari and GOES-E and -W using  
1170 the same FTA algorithm originally developed for Meteosat SEVIRI (Roberts and  
1171 Wooster, 2008; Wooster *et al.*, 2015; Xu *et al.*; 2017; 2021a). Similarly, the availability  
1172 of Landsat and Sentinel-2 imagery having pixel sizes in the tens of meters provides  
1173 detailed SWIR-based AF detection that may complement coarser spatial resolution but  
1174 more frequently available AF products, if only initially for validation of the latter. The  
1175 increasing number of very high spatial resolution (1-3 m) sensors should also be  
1176 evaluated for their potential use in AF detection. Development of additional ancillary  
1177 datasets, such as those related to fuel load per unit area, and biome, season and fuel-  
1178 moisture dependent trace gas and aerosol emissions factors (EFs), is required to further  
1179 improve fire emissions estimation.

1180

## 1181 **10.2 EO Sensor and Mission Priorities**

1182 This review has reiterated that to provide optimum data for AF remote sensing, a  
1183 typical sensor requires co-registered channels in the MIR (3 – 5  $\mu\text{m}$ ) and LWIR (8 – 14  
1184  $\mu\text{m}$ ), a co-located VIS or NIR channel to aid daytime masking of false alarms and cloud.  
1185 The exact spectral placement of each channel is less prescriptive, but for example the  
1186 3.959  $\mu\text{m}$  “fire channel” of MODIS was selected due to its relative insensitivity to  
1187 atmospheric water vapor absorption and avoidance of the  $\text{CO}_2$  absorption window  
1188 beyond  $\sim 4 \mu\text{m}$  (Kaufman *et al.*, 1998). Of key importance for FRP retrieval are MIR  
1189 measurements across a sufficient dynamic range to provide good quality, unsaturated  
1190 data over the highest intensity and/or largest fires, as well as over the ambient  
1191 temperature background. Without the former, the FRP of the most strongly emitting  
1192 fires cannot be gauged, and without the latter the AF pixels themselves may not even be  
1193 reliably detected. The required upper end of the MIR channel dynamic range needs to  
1194 be set according to the sensors ground pixel footprint area, since the same fire will form  
1195 a greater proportion of a smaller rather than larger pixel (MODIS 1  $\text{km}^2$  pixels have  $\sim$   
1196 500 K saturation temperature *vs.* ABI 4  $\text{km}^2$  pixels have  $\sim 400 \text{ K}$ ). For the 60 m spatial  
1197 resolution MIR band of the proposed Hyperspectral Infrared Imager (HyspIRI) payload,  
1198 Realmuto *et al.* (2015) specified a 1200 K saturation temperature. As with MODIS and  
1199 SLSTR, such wide dynamic ranges sometimes require two MIR detectors, or one  
1200 detector operating with dual integration times or gain settings (e.g. BIRD HSRS and  
1201 VIIRS). Other beneficial sensor attributes include limiting pixel area growth across the  
1202 swath (as done with VIIRS and SLSTR; Schroeder *et al.*, 2014; Xu *et al.*, 2021b), a SWIR  
1203 channel operating at night to aid hotspot detection, discrimination of fires from higher  
1204 temperature targets such as gas-flares, and FRP estimation from the latter (Fisher and  
1205 Wooster, 2018; 2019). SWIR wavebands centered around 2.2  $\mu\text{m}$  appear most effective,  
1206 and night-time use of a broad day-night (low light level) band (0.5 - 0.9  $\mu\text{m}$ ) similar to  
1207 that of VIIRS can also be considered. SWIR-based AF detection is also possible by day if  
1208 ground pixel footprints are small enough.

1209 High temporal resolution AF data is required for operational fire monitoring,  
1210 warning and fire-fighting applications, and to provide the most reliable estimation of  
1211 FRE via FRP temporal integration. GEO systems meet this goal, with the newest such as  
1212 Himawari (Bessho *et al.* 2016, Xu *et al.* 2017), Meteosat Second Generation (soon to be

1213 superseded by Meteosat Third Generation [MTG]; Roberts and Wooster, 2008), GEO-  
1214 KOMPSAT-2A and Feng-Yun 4A (Yang *et al.* 2017), and GOES-R (Schmit *et al.* 2017; Xu  
1215 *et al.* 2017; 2021) including MIR bands having suitably extended dynamic ranges, and  
1216 offering full-disk temporal resolutions as high as 10 minutes. However, their larger pixel  
1217 areas result in minimum FRP detection limits typically at least 4× higher than from the  
1218 nadir views of LEO sensors – so they generally cannot detect a substantial number of  
1219 fires that MODIS type sensors would identify if they viewed the same location at the  
1220 same time. MTG will offer 1 km data every 2.5 minutes over some areas, a first for the  
1221 AF application, and even in densely populated Europe this may provide sufficient  
1222 capability to usefully detect a significant number of newly ignited fires in advance of  
1223 public call ins. Use of highly elliptical orbits could be explored to provide a high latitude,  
1224 high temporal resolution AF capability. An achievable future GEO goal that would cover  
1225 many of the applications supported by current LEO systems would be 500 m spatial  
1226 resolution geostationary-based AF detection, and the Chinese Meteorological Agency  
1227 (CMA) GF4 GEO satellite already includes a 400m MIR channel that demonstrates this  
1228 is possible (Lu *et al.*, 2020).

1229  
1230 An option to provide high spatial detail, low commission error AF data at increased  
1231 temporal resolutions is via constellations of LEO systems placed to cover different  
1232 overpass times. LEO capabilities continue to improve, and compared to MODIS  
1233 Sentinel-3 SLSTR offers a somewhat improved AF detection sensitivity due to its on  
1234 average smaller pixel footprint area (Xu *et al.*, 2020; 2021; **Figure 3**), whilst VIIRS' 375  
1235 m data offers a sensitivity around 10× better (Schroeder *et al.*, 2014; Zhang *et al.*, 2017).  
1236 Going beyond the spatial resolution of VIIRS may provide diminishing returns, since the  
1237 latter can already identify active areas of combustion of < 20 m<sup>2</sup>, and over some  
1238 landscapes high AF errors of commission can result from the IR clutter present in very  
1239 finely detailed thermal imagery (Schroeder *et al.*, 2014; Zhang *et al.*, 2017).  
1240 Performance trade-offs between the existing style of often larger satellites using cooled  
1241 sensor technology and lower cost smaller missions that might enable lower-cost  
1242 constellation development, possibly using uncooled detectors if their performance can  
1243 be demonstrated (e.g. WildFireSat; Johnston *et al.* 2020), should be examined.

1244

1245

1246 **10.3 Other Research Priorities**

1247 Beyond datasets and sensors, there remain several primacies for ongoing  
1248 research in AF remote sensing. These include a better understanding of errors and  
1249 uncertainties in AF detection, FRP retrieval and fire emissions estimation, both spatially  
1250 (e.g. by biome, temporally (e.g. diurnally, seasonally) and with respect to different  
1251 sensors, products and observational (e.g. atmospheric and view angle) effects.  
1252 Validation of AF products remains challenging, due to the ephemeral and dynamic  
1253 nature of fire and to difficulties in obtaining co-located simultaneous and independent  
1254 reference observations. On a global scale this has been limited to joint use of ASTER and  
1255 Terra MODIS (see Section 1), and with Terra nearing its end of life there is a need to  
1256 develop a validation strategy covering a wider array of instruments and times of day.  
1257 Similarly, a uniform protocol to validate spaceborne FRP retrievals is required,  
1258 particularly as it is a designated GCOS ECV and one which is still at the lowest  
1259 validation stage according to the CEOS LPV validation hierarchy. Understanding the  
1260 lower FRP components of a regions fire regime and how this is included or excluded by  
1261 different AF data products remains important, as are ways to adjust for this when  
1262 necessary. The ability to map fireline rates of spread remains a goal for many fire  
1263 management applications, as is the need to further promote assimilation of NRT AF  
1264 data into time-coupled weather-fire behavior modelling frameworks (Cohen and  
1265 Schroeder, 2013). Research on the conversion between FRP, FRE and fuel consumption,  
1266 trace gas and aerosol emissions continues to be a priority, as does the reconciling of  
1267 such estimates with those from alternative (e.g. burned area) based approaches. Finally,  
1268 the accuracy and usefulness of EO methods for flaming/smouldering fire discrimination  
1269 - including via use of phenomena such as detection of landscape fire potassium emission  
1270 lines - needs to be further examined, as does the need and ability to optimize any  
1271 applied emissions factors used in subsequent smoke emissions calculations.

1272

1273 **11. Summary and Conclusion**

1274 Observing landscape fires from space has a strong heritage, stretching back to the  
1275 1980's with NOAA AVHRR. Since then, satellite active fire (AF) data have become very

widely used by scientists and government agencies, and the number of spaceborne sensors equipped with measurement capabilities relevant to the AF application, including with ‘fire-optimized’ thermal channel dynamic ranges, has greatly increased. The NASA MODIS AF product suite is the most widely utilized, and the ease of access to these and other AF data through numerous data portals has proliferated beyond science to allow routine monitoring and reporting - as evidenced by their deployment by the media during the recent [2019] Amazonian fire activity increase (Kelley *et al.*, 2021) and during the 2019/2020 Australian black Summer bushfires (Abram *et al.*, 2021). Although these recent events have highlighted the relevance and importance of satellite AF products (e.g. Escobar, 2019), they have also reinforced the need for the community of data producers to more clearly communicate the limitations as well as benefits of each AF product, so as to reduce interpretation inaccuracies.

AF products have evolved from reporting the timing and location of actively burning fires to now include measures such as fire effective temperature, area and fire radiative power (FRP). Near real-time (NRT) EO data streams have allowed the FRP method to be used to deliver smoke emissions source strength information to a variety of atmospheric modelling systems, for example in support air quality forecasting. Future satellite missions, including higher spatial resolution GEO systems and increased numbers of AF-capable LEO systems, including the future possibly of small-satellite constellations, provide further opportunities for advancing both science and operational applications as their performance evolves. A key constraint remains the scarcity of reference data suitable for validating contemporaneous AF detections and FRP retrievals. Communities such as GOFC/GOLD and CEOS LPV are encouraged to continue to lobby space agencies to develop and launch missions that include sensors whose characteristics are optimized for the AF application, and often only relatively small adjustments to the initially planned characteristics are required – as was the case for example with Sentinel-3 SLSTR and Meteosat Third Generation. Looking forward, continuing climate and environmental change may potentially shift certain drivers of landscape fire (Rogers *et al.*, 2020). Apparent policy or policy enforcement shifts appear able to rapidly alter fire characteristics over large regions (Sembhi *et al.*, 2020), and the health impacts of the poor air quality that can come with landscape burning is a growing

1307 concern. We can therefore expect the relevance and importance of satellite AF remote  
1308 sensing to continue to grow.

1309

1310

1311 **Acknowledgments**

1312 M.W. contributed to this review with support from the Leverhulme Centre for Wildfires,  
1313 Environment and Society (Leverhulme Trust grant number RC-2018-023), NERC  
1314 National Capability funding to the National Centre for Earth Observation  
1315 (NE/R016518/1), and CEOS Wildfire Pilot. The National Science Foundation supported  
1316 A.S. under award DMS-1520873, and C.I. is also grateful for partial support received  
1317 from the NOAA Educational Partnership Program under Agreement No.  
1318 #NA16SEC4810006. This review is an official output from the Global Observation of  
1319 Forest Cover/Global Observation of Landcover Dynamics (GOFC/GOLD) Fire  
1320 Programme (<https://gofcgold.org/>).

1321

1322 **References**

1323 Abram, N.J., Henley, B.J., Gupta, A.S., Lippmann, T.J., Clarke, H., Dowdy, A.J.,  
1324 Sharples, J.J., Nolan, R.H., Zhang, T., Wooster, M.J. and Wurtzel, J.B., 2021.  
1325 Connections of climate change and variability to large and extreme forest fires in  
1326 southeast Australia. *Communications Earth & Environment*, 2(1), pp.1-17.

1327

1328 Alexander, M.E. (1982) Fire behavior in aspen slash fuels as related to the Canadian Fire  
1329 Weather Index. *Canadian Journal of Forest Research*. 12. 4. 1028-1029.

1330

1331 Amici, S., Wooster, M.J. and Piscini, A., 2011. Multi-resolution spectral analysis of  
1332 wildfire potassium emission signatures using laboratory, airborne and spaceborne  
1333 remote sensing. *Remote Sensing of Environment*, 115(8), pp.1811-1823.

1334

1335 Amraoui, M., DaCamara, C.C. and Pereira, J.M.C., 2010. Detection and monitoring of  
1336 African vegetation fires using MSG-SEVIRI imagery. *Remote sensing of*  
1337 *Environment*. 114. 5.1038-1052.

1338

1339 Andela, N., Kaiser, J.W., van der Werf, G.R., & Wooster, M.J. (2015). New fire diurnal  
1340 cycle characterizations to improve fire radiative energy assessments made from MODIS  
1341 observations. *Atmospheric Chemistry and Physics*, 15, 8831-8846

1342

1343 Andela, N., Morton, D.C., Giglio, L., Paugam, R., Chen, Y., Hantson, S., Werf, G.R. and  
1344 Randerson, J.T., 2019. The Global Fire Atlas of individual fire size, duration, speed and  
1345 direction. *Earth System Science Data*, 11(2), pp.529-552.

1346

1347 Atwood, E.C., Englhart, S., Lorenz, E., Halle, W., Wiedemann, W. and Siegert, F., 2016.  
1348 Detection and characterization of low temperature peat fires during the 2015 fire  
1349 catastrophe in Indonesia using a new high-sensitivity fire monitoring satellite sensor  
1350 (FireBird). *PloS one*, 11(8).

1351

- 1352 Àgueda, A., Pastor, E., Pérez, Y. and Planas, E. (2010) Experimental study of the  
1353 emissivity of flames resulting from the combustion of forest fuels. *International Journal*  
1354 *of Thermal Sciences*. 49. 3. 543-554.
- 1355
- 1356 Aragao, L.E.O.C., & Shimabukuro, Y.E. (2010). The Incidence of Fire in Amazonian  
1357 Forests with Implications for REDD. *Science*. 328. 1275-1278
- 1358
- 1359 Archibald, S., Roy, D.P., van Wilgen, B.W., & Scholes, R.J. (2009). What limits fire? An  
1360 examination of drivers of burnt area in Southern Africa. *Global Change Biology*. 15.  
1361 613-630.
- 1362
- 1363 Arino, O., Rosaz, J.-M., and Goloub, P. (1999). The ATSR world fire atlas: A synergy  
1364 with "Polder" aerosol products. *Earth Observation Quarterly*, no 64.
- 1365
- 1366
- 1367 Arino, O., Casadio, S., & Serpe, D. (2012). Global night-time fire season timing and fire  
1368 count trends using the ATSR instrument series. *Remote Sensing of Environment*. 116.  
1369 226-238.
- 1370
- 1371 Bessho, K., Date, K., Hayashi, M., Ikeda, A., Imai, T., Inoue, H., Kumagai, Y., Miyakawa,  
1372 T., Murata, H., Ohno, T. and Okuyama, A., 2016. An introduction to Himawari-8/9—  
1373 Japan's new-generation geostationary meteorological satellites. *Journal of the*  
1374 *Meteorological Society of Japan. Ser. II*, 94(2), pp.151-183.
- 1375
- 1376 Bond, W.J., & Keeley, J.E. 2005. Fire as a global 'herbivore': the ecology and evolution  
1377 of flammable ecosystems. *Trends in Ecology & Evolution*, 20, 387-394, DOI  
1378 10.1016/j.tree.2005.04.025
- 1379
- 1380 Boschetti L. and Roy, D.P. (2009) Strategies for the fusion of satellite fire radiative  
1381 power with burned area data for fire radiative energy derivation, *Journal of Geophysical*  
1382 *Research Atmospheres*. 114. D20302, doi:10.1029/2008JD011645.
- 1383

- 1384 Boschetti, L., Roy, D.P. and Justice, C.O., 2009. International Global Burned Area  
1385 Satellite Product Validation Protocol Part I—production and standardization of  
1386 validation reference data. *Committee on Earth Observation Satellites: Maryland, MD,*  
1387 *USA*, pp.1-11.
- 1388
- 1389
- 1390 Bowman, D.M., Balch, J.K., Artaxo, P., Bond, W.J., Carlson, J.M., Cochrane, M.A.,  
1391 D'Antonio, C.M., DeFries, R.S., Doyle, J.C., Harrison, S.P. and Johnston, F.H. (2009)  
1392 Fire in the Earth system. *Science*. 324. 5926. 481-484.
- 1393
- 1394 Briess, K., Jahn, H., Lorenz, E., Oertel, D., Skrbek, W. and Zhukov, B., 2003. Fire  
1395 recognition potential of the bi-spectral Infrared Detection (BIRD)  
1396 satellite. *International Journal of Remote Sensing*. 24. 4. 865-872.
- 1397
- 1398 Brönnimann, S., Volken, E., Lehmann, K. and Wooster, M., 2009. Biomass burning  
1399 aerosols and climate. A 19th century perspective. *Meteorologische Zeitschrift*  
1400 (Berlin), 18.
- 1401
- 1402 Cahoon Jr, D.R., Stocks, B.J., Levine, J.S., Cofer III, W.R. and O'Neill, K.P., 1992.  
1403 Seasonal distribution of African savanna fires. *Nature*, 359(6398), p.812.
- 1404
- 1405 Cahoon, D.R., Stocks, B.J., Alexander, M.E., Baum, B.A., & Goldammer, J.G. (2000).  
1406 Wildland Fire Detection from Space: Theory and Application. In J.L. Innes, M.  
1407 Beniston, & M.M. Verstraete (Eds.), *Biomass Burning and Its Inter-Relationships with*  
1408 *the Climate System* (pp. 151-169). Dordrecht: Springer Netherlands
- 1409
- 1410 Cheney, P. and Sullivan, A. eds., 2008. *Grassfires: fuel, weather and fire behaviour*.  
1411 Csiro Publishing.
- 1412
- 1413 Chuvieco, E., Giglio, L., & Justice, C. (2008). Global characterization of fire activity:  
1414 toward defining fire regimes from Earth observation data. *Global Change Biology*,  
1415 1488-1502

- 1416
- 1417 Chuvieco, E., Mouillot, F., van der Werf, G.R., San Miguel, J., Tanasse, M., Koutsias, N.,  
1418 García, M., Yebra, M., Padilla, M., Gitas, I. and Heil, A. (2019) Historical background  
1419 and current developments for mapping burned area from satellite Earth  
1420 observation. *Remote Sensing of Environment*. 225. 45-64.
- 1421
- 1422 Coheur, P.F., Clarisse, L., Turquety, S., Hurtmans, D. and Clerbaux, C. (2009) IASI  
1423 measurements of reactive trace species in biomass burning plumes. *Atmospheric*  
1424 *Chemistry and Physics*. 9. 15. 5655-5667
- 1425
- 1426 Csiszar, I., & Sullivan, J. (2002). Recalculated pre-launch saturation temperatures of the  
1427 AVHRR 3.7  $\mu$ m sensors on board the TIROS-N to NOAA-14 satellites. *International*  
1428 *Journal of Remote Sensing*, 23(24), 5271-5276.
- 1429
- 1430 Csiszar, I., A. Abuelgasim, Z. Li, J. Jin, R. Fraser, and W.-M. Hao, 2003, Interannual  
1431 changes of active fire detectability in North America from long-term records of the  
1432 advanced very high resolution radiometer, *Journal of Geophysical Research*, 108(D2),  
1433 4075.
- 1434
- 1435 Csiszar, I., Denis, L., Giglio, L., Justice, C., & Hewson, J. (2005). Global fire activity  
1436 from two years of MODIS data. *International Journal of Wildland Fire*. 117-130
- 1437
- 1438 Csiszar I.A., Justice C.O., Goldammer J.G., Lynham T., de Groot W.J., Prins E.M.,  
1439 Elvidge C.D., Oertel D. , Lorenz E., Bobbe T., Quayle B., Davies D., Roy D., Boschetti L.,  
1440 Korontzi S., Ambrose S., Stephens G. (2013) The GOFC/GOLD Fire Mapping and  
1441 Monitoring theme: assessment and strategic plans. In Qu, J.J.; Sommers, W.; Yang, R.;  
1442 Riebau, A.; Kafatos, M. (Eds.) *Remote Sensing Modeling and Applications to Wildland*  
1443 *Fires*. Springer-Verlag, co-published with Tsinghua University Press, 2013, 550 pp.  
1444 ISBN 978-3-642-32529-8
- 1445
- 1446 Csiszar, I., Schroeder, W., Giglio, L., Ellicott, E., Vadrevu, K.P., Justice, C.O., and Wind,  
1447 B. (2014). Active fires from the Sumi NPP Visible Infrared Imaging Radiometer Suite:

- 1448 Product status and first evaluation results. *Journal of Geophysical Research: Atmospheres*. 119. doi: 10.1002/2013JD020453
- 1450
- 1451 Darmenov, A. and da Silva. A. (2015): The quick fire emissions dataset (QFED)–  
1452 documentation of versions 2.1, 2.2 and 2.4, NASA Technical Report Series on Global  
1453 Modeling and Data Assimilation, NASA TM-2015-104606, 38.
- 1454
- 1455 Davies, D.K., Murphy, K.J., Michael, K., Becker-Reshef, I., Justice, C.O., Boller, R.,  
1456 Braun, S., Schmaltz, J., Wong, M., Pasch, A., Dye, T., da Silva, A., Goodman, M., Morin,  
1457 P. (2014) The Use of NASA LANCE Imagery and Data for Near Real-Time Application.  
1458 In: Lippitt C., Stow D., Coulter L.(Eds) *Time Sensitive Remote Sensing*. Springer Press.  
1459 165-182.
- 1460
- 1461 Dennison, P.E., Charoensiri, K., Roberts, D.A., Peterson, S.H. and Green, R.O., 2006.  
1462 Wildfire temperature and land cover modeling using hyperspectral data. *Remote  
1463 Sensing of Environment*, 100(2), pp.212-222.
- 1464
- 1465 Devineau, J.L., Fournier, A., & Nignan, S. (2010). Savanna fire regimes assessment with  
1466 MODIS fire data: Their relationship to land cover and plant species distribution in  
1467 western Burkina Faso (West Africa). *Journal of Arid Environments*. 74. 1092-1101
- 1468
- 1469 Di Bella, C.M., Jobbagy, E.G., Paruelo, J.M., & Pinnock, S. (2006). Continental fire  
1470 density patterns in South America. *Global Ecology and Biogeography*. 15, 192-199
- 1471
- 1472 Di Biase, V. and Laneve, G. (2018) Geostationary sensor based forest fire detection and  
1473 monitoring: An improved version of the SFIDE algorithm. *Remote Sensing*. 10. 5. 741.
- 1474
- 1475 Dozier, J. (1981). A method for satellite identification of surface temperature fields of  
1476 subpixel resolution. *Remote Sensing of Environment*. 11. 221-229.
- 1477

- 1478 Duff, T.J. and Penman, T.D. (2021). Determining the likelihood of asset destruction  
1479 during wildfires: modelling house destruction with fire simulator outputs and local-scale  
1480 landscape properties. *Safety Science*, 139, 105196.  
1481
- 1482 Dwyer, E., Pinnock, S., Gregoire, J.M., & Pereira, J.M.C. (2000). Global spatial and  
1483 temporal distribution of vegetation fire as determined from satellite observations.  
1484 *International Journal of Remote Sensing*, 21, 1289-1302  
1485
- 1486 Eidenshink, J.C. and Faundeen, J.L. (1994) The 1 km AVHRR global land data set: first  
1487 stages in implementation. *International Journal of Remote Sensing*. 15. 17. 3443-3462.  
1488
- 1489 Ellicott, E., Vermote, E., Giglio, L., & Roberts, G. (2009). Estimating biomass consumed  
1490 from fire using MODIS FRE. *Geophysical Research Letters*. 36. 13.  
1491 <https://doi.org/10.1029/2009GL038581>  
1492
- 1493 Ellyett, C.D. and Fleming, A.W., 1974. Thermal infrared imagery of the Burning  
1494 Mountain coal fire. *Remote Sensing of Environment*, 3(1), pp.79-86.  
1495
- 1496 Elvidge, C. D., Kroehl, H. W., Kihn, E. A., Baugh, K. E., Davis, E. R., and Hao, W. M.  
1497 (1996). Algorithm for the retrieval of fire pixels from DMSP operational linescan system  
1498 data. In J. S. Levine (Ed.), *Biomass burning and global change: Remote sensing,*  
1499 *modeling and inventory development, and biomass burning in Africa*, Vol.1 (pp. 73–85).  
1500 Cambridge: MIT Press.  
1501
- 1502 Elvidge, C. D., Zhizhin, M., Hsu, F.-C., and Baugh, K. E. (2013). VIIRS nightfire:  
1503 Satellite pyrometry at night. *Remote Sensing*. 5, 4423-4449. doi: 10.3390/rs5094423.  
1504
- 1505 Elvidge, C.D., Zhizhin, M., Hsu, F-C., Baugh, K., Khomarudin, M. R., Vetrata, Y., Sofan,  
1506 P., Suwarsono, and Hilman, D. (2015) Long-wave infrared identification of moldering  
1507 peat fires in Indonesia with nighttime Landsat data. *Environmental Research Letters*.  
1508 10.065002. doi:10.1088/1748-9326/10/6/065002  
1509

- 1510 Escobar, H. (2019). Amazon fires clearly linked to deforestation, scientists say. *Science*,  
1511 6456, 853-853.
- 1512
- 1513 Fisher, D. and Wooster, M. (2018) Shortwave IR Adaption of the Mid-Infrared Radiance  
1514 Method of Fire Radiative Power (FRP) Retrieval for Assessing Industrial Gas Flaring  
1515 Output. *Remote Sensing*. 10. 2. p.305.
- 1516
- 1517 Fisher, D. and Wooster, M.J. (2019) Multi-decade global gas flaring change inventoried  
1518 using the ATSR-1, ATSR-2, AATSR and SLSTR data records. *Remote Sensing of*  
1519 *Environment*, 232, p.111298.
- 1520
- 1521 Fisher, D., Wooster, M.J., Xu, W., Thomas, G. and Lestari, P., 2020. Top-Down  
1522 Estimation of Particulate Matter Emissions from Extreme Tropical Peatland Fires Using  
1523 Geostationary Satellite Fire Radiative Power Observations. *Sensors*, 20(24), p.7075.
- 1524
- 1525 Filizzola, C., Corrado, R., Marchese, F., Mazzeo, G., Paciello, R., Pergola, N. and  
1526 Tramutoli, V. (2017) RST-FIRES, an exportable algorithm for early-fire detection and  
1527 monitoring: Description, implementation, and field validation in the case of the MSG-  
1528 SEVIRI sensor. *Remote Sensing of Environment*, 192, pp.e2-e25.
- 1529
- 1530 Flannigan, M. D. and Vonder Haar, T. H. (1986). Forest fire monitoring using the  
1531 NOAA satellite AVHRR. *Canadian Journal of Forest Research*. 16(5). 975-982.
- 1532
- 1533 Flasse, S. P., and Ceccato, P. (1996). A contextual algorithm for AVHRR fire detection.  
1534 *International Journal of Remote Sensing*. 17. 419-424.
- 1535
- 1536 Freeborn, P.H., Wooster, M.J., Hao, W.M., Ryan, C.A., Nordgren, B.L., Baker, S.P. and  
1537 Ichoku, C. (2008) Relationships between energy release, fuel mass loss, and trace gas  
1538 and aerosol emissions during laboratory biomass fires. *Journal of Geophysical*  
1539 *Research: Atmospheres*, 113(D1).
- 1540

- 1541 Freeborn, P.H., Wooster, M.J., Roberts, G., Malamud, B.D. and Xu, W. (2009)  
1542 Development of a virtual active fire product for Africa through a synthesis of  
1543 geostationary and polar orbiting satellite data. *Remote Sensing of Environment*. 113. 8.  
1544 1700-1711.
- 1545
- 1546 Freeborn, P. H., Wooster, M. J., Roberts, G. (2011) Addressing the spatiotemporal  
1547 sampling design of MODIS to provide estimates of the fire radiative energy emitted from  
1548 Africa. *Remote Sensing of Environment*. 115. 2. 475 – 489
- 1549
- 1550 Freeborn, P.H., Wooster, M.J., Roy, D.P. and Cochrane, M.A. (2014a). Quantification of  
1551 MODIS fire radiative power (FRP) measurement uncertainty for use in satellite - based  
1552 active fire characterization and biomass burning estimation. *Geophysical Research  
1553 Letters*, 41, 1988-1994.
- 1554
- 1555 Freeborn, P.H., Cochrane, M.A., & Wooster, M.J. (2014b). A Decade Long, Multi-Scale  
1556 Map Comparison of Fire Regime Parameters Derived from Three Publically Available  
1557 Satellite-Based Fire Products: A Case Study in the Central African Republic. *Remote  
1558 Sensing*, 6, 4061-4089
- 1559
- 1560 Freeborn, P.H., Jolly, W.M., & Cochrane, M.A. (2016). Impacts of changing fire weather  
1561 conditions on reconstructed trends in US wildland fire activity from 1979 to 2014.  
1562 *Journal of Geophysical Research-Biogeosciences*. 121. 2856-2876
- 1563
- 1564 Friedlingstein, P., O'sullivan, M., Jones, M.W., Andrew, R.M., Hauck, J., Olsen, A.,  
1565 Peters, G.P., Peters, W., Pongratz, J., Sitch, S. and Le Quéré, C. (2020). Global carbon  
1566 budget 2020. *Earth System Science Data*, 12, 3269-3340.
- 1567
- 1568 GCOS, 2016. The global observing system for climate: Implementation needs, GCOS -  
1569 200. [https://library.wmo.int/doc\\_num.php?explnum\\_id=3417](https://library.wmo.int/doc_num.php?explnum_id=3417) (last accessed March  
1570 2021)
- 1571

- 1572 Giglio, L. (2007). Characterization of the tropical diurnal fire cycle using VIRS and  
1573 MODIS observations. *Remote Sensing of Environment*. 407-421
- 1574
- 1575 Giglio, L. and Kendall, J.D. (2001) Application of the Dozier retrieval to wildfire  
1576 characterization: a sensitivity analysis. *Remote Sensing of Environment*, 77. 1. 34-49.
- 1577
- 1578 Giglio, L., Kendall, J.D., and Justice, C.O. (1999). Evaluation of global fire detection  
1579 algorithms using simulated AVHRR infrared data. *International Journal of Remote  
1580 Sensing*. 20(10). 1947-1985.
- 1581
- 1582 Giglio, L., Kendall, J.D. and Tucker, C.J. (2000) Remote sensing of fires with the TRMM  
1583 VIRS. *International Journal of Remote Sensing*. 21. 1. 203-207.
- 1584
- 1585 Giglio, L., Descloitres, J., Justice, C.O., and Kaufman, Y.J. (2003). An enhanced  
1586 contextual fire detection algorithm for MODIS. *Remote Sensing of Environment*. 87.  
1587 273-282.
- 1588
- 1589 Giglio, L., Csiszar, I., & Justice, C. (2006). Global distribution and seasonality of active  
1590 fires as observed with the Terra and Aqua Moderate Resolution Imaging  
1591 Spectroradiometer (MODIS) sensors. *Journal of Geophysical Research-Biogeosciences*.  
1592 111. G2. <https://doi.org/10.1029/2005JG000142>
- 1593
- 1594 Giglio, L., Csiszar, I., Restás, Á., Morisette, J. T., Schroeder, W., Morton, D., and Justice,  
1595 C. O. (2008). Active fire detection and characterization with the Advanced Spaceborne  
1596 Thermal Emission and Reflection Radiometer (ASTER). *Remote Sensing of  
1597 Environment*. 112. 3055-3063.
- 1598
- 1599 Giglio, L., J. T. Randerson, G. R. Van der Werf, P. S. Kasibhatla, G. J. Collatz, D. C.  
1600 Morton, and R. S. DeFries. (2010) Assessing variability and long-term trends in burned  
1601 area by merging multiple satellite fire products. *Biogeosciences*. 7. 3. 1171-1186.
- 1602

- 1603 Giglio, L., Randerson, J. T., and van der Werf, G. R., (2013), Analysis of daily, monthly,  
1604 and annual burned area using the fourth generation Global Fire Emissions Database  
1605 (GFED4). *Journal of Geophysical Research: Biogeosciences*, 118.
- 1606
- 1607 Giglio, L., & Schroeder, W. (2014). A global feasibility assessment of the bi-spectral fire  
1608 temperature and area retrieval using MODIS data. *Remote Sensing of Environment*.  
1609 152. 166-173
- 1610
- 1611 Giglio, L., Schroeder, W., and Justice, C.O. (2016). The collection 6 MODIS active fire  
1612 detection algorithm and fire products. *Remote Sensing of Environment*. 178. 31-41.
- 1613
- 1614 Giglio, L., Boschetti, L., Roy, D.P., Humber, M.L., Justice, C.O. (2018) The Collection 6  
1615 MODIS burned area mapping algorithm and product. *Remote Sensing of Environment*.  
1616 217. 72-85.
- 1617
- 1618 Giglio, L. and Roy, D.P. (2020). On the outstanding need for a long-term, multi-decadal,  
1619 validated and quality assessed record of global burned area: caution in the use of  
1620 Advanced Very High Resolution Radiometer data, *Science of Remote Sensing*. 2,  
1621 p.100007.
- 1622
- 1623 Gill, A.M. (1975) Fire and the Australian flora: a review. *Australian Forestry*. 38. 4-25
- 1624
- 1625 Gregoire, J.M., and Simonetti, D. (2010). Interannual Changes of Fire Activity in the  
1626 Protected Areas of the SUN Network and Other Parks and Reserves of the West and  
1627 Central Africa Region Derived from MODIS Observations. *Remote Sensing*. 2. 446-463
- 1628
- 1629 Hall, J.V., Zhang, R., Schroeder, W., Huang, C. and Giglio, L., 2019. Validation of GOES-  
1630 16 ABI and MSG SEVIRI active fire products. *International Journal of Applied Earth  
1631 Observation and Geoinformation*, 83, p.101928.
- 1632

- 1633 Hally, B., Wallace, L., Reinke, K. and Jones, S. (2017) A broad-area method for the  
1634 Diurnal characterisation of upwelling medium wave infrared radiation. *Remote*  
1635 *sensing*. 9. 2. 167.
- 1636
- 1637 Hantson, S., Padilla, M., Corti, D., & Chuvieco, E. (2013). Strengths and weaknesses of  
1638 MODIS hotspots to characterize global fire occurrence. *Remote Sensing of*  
1639 *Environment*. 131. 152-159.
- 1640
- 1641 Henderson S.B., Burkholder, B., Jackson, P.L., Brauer, M., Ichoku, C. (2008) Use of  
1642 MODIS products to simplify and evaluate a forest fire plume dispersion model for PM10  
1643 exposure assessment. *Atmospheric Environment*. 42. 8524-8532.
- 1644
- 1645 Hirsch, S.N. (1965) Airborne infrared mapping of forest fires. *Fire Technology*, 1.4. 288-  
1646 294.
- 1647
- 1648 Hirsch, K.G., 1991. A chronological overview of the 1989 fire season in Manitoba. *The*  
1649 *Forestry Chronicle*, 67. 4. 358-365.
- 1650
- 1651 Hirsch, E. and Koren, I., 2021. Record-breaking aerosol levels explained by smoke  
1652 injection into the stratosphere. *Science*, 371(6535), pp.1269-1274.
- 1653
- 1654 Huijnen, V., Wooster, M.J., Kaiser, J.W., Gaveau, D.L., Flemming, J., Parrington, M.,  
1655 Inness, A., Murdiyarso, D., Main, B. and van Weele, M., 2016. Fire carbon emissions  
1656 over maritime southeast Asia in 2015 largest since 1997. *Scientific reports*, 6(1), pp.1-8.
- 1657
- 1658 Hyer, E.J., Reid, J.S., Prins, E.M., Hoffman, J.P., Schmidt, C.C., Miettinen, J.I., and  
1659 Giglio, L. (2013). Patterns of fire activity over Indonesia and Malaysia from polar and  
1660 geostationary satellite observations. *Atmospheric Research*. 122. 504-519
- 1661
- 1662 Ichoku, C., Remer, L.A., Kaufman, Y.J., Levy, R., Chu, D.A., Tanré, D. and Holben, B.N.  
1663 (2003) MODIS observation of aerosols and estimation of aerosol radiative forcing over

1664 southern Africa during SAFARI 2000. *Journal of Geophysical Research: Atmospheres*. 108 (D13).

1666

1667 Ichoku, C., Kaufman, Y.J. (2005) A method to derive smoke emission rates from MODIS  
1668 fire radiative energy measurements. *IEEE Trans. Geosci. Rem. Sensing* 43(11), 2636-  
1669 2649.

1670

1671 Ichoku, C., Giglio, L., Wooster, M.J., & Remer, L.A. (2008). Global characterization of  
1672 biomass-burning patterns using satellite measurements of fire radiative energy. *Remote  
1673 Sensing of Environment*. 112. 2950-2962

1674

1675 Ichoku, C. and Ellison, L. (2014) Global top-down smoke aerosol emissions estimation  
1676 using satellite fire radiative power measurements. *Atmospheric Chemistry & Physics*,  
1677 14(13), pp.6643-6667.

1678

1679 Johnston, J.M., Wooster, M.J. and Lynham, T.J. (2014) Experimental confirmation of  
1680 the MWIR and LWIR grey body assumption for vegetation fire flame  
1681 emissivity. *International Journal of Wildland Fire*. 23. 4.463-479.

1682

1683 Johnston, J.M., Wheatley, M.J., Wooster, M.J., Paugam, R., Davies, G.M. and DeBoer,  
1684 K.A. (2018) Flame-Front Rate of Spread Estimates for Moderate Scale Experimental  
1685 Fires Are Strongly Influenced by Measurement Approach. *Fire*. 1. 1. p.16.

1686

1687

1688 Johnston, F.H., Henderson, S.B., Chen, Y., Randerson, J.T., Marlier, M., DeFries, R.S.,  
1689 Kinney, P., Bowman, D.M. and Brauer, M., 2012. Estimated global mortality attributable  
1690 to smoke from landscape fires. *Environmental health perspectives*, 120(5), pp.695-701.

1691

1692 Johnston, J.M., Johnston, L.M., Wooster, M.J., Brookes, A., McFayden, C. and Cantin,  
1693 A.S., 2018. Satellite detection limitations of sub-canopy smouldering wildfires in the  
1694 North American Boreal Forest. *Fire*, 1(2), p.28.

1695

- 1696 Jordan, N.S., Ichoku, C. and Hoff, R.M., 2008. Estimating smoke emissions over the US  
1697 Southern Great Plains using MODIS fire radiative power and aerosol  
1698 observations. *Atmospheric Environment*, 42(9), pp.2007-2022.
- 1699
- 1700 Justice, C.O., Malingreau, J.P. and Setzer, A.W. (1993) Satellite remote sensing of fires-  
1701 Potential and limitations. *Fire in the environment- The ecological, atmospheric, and*  
1702 *climatic importance of vegetation fires*. Chichester, United Kingdom, John Wiley &  
1703 Sons, Ltd., 1993,, pp.77-88.
- 1704
- 1705 Justice, C., Vermote, E., Townshend, J., Defries, R., Roy, D., Hall, D., Salomonson, V.,  
1706 Privette, J., Riggs, G., Strahler, A., Lucht, W., Myneni, R., Knyazikhin, Y., Running, S.,  
1707 Nemani, R., Wan, Z., Huete, A., van Leeuwen, W., Wolfe, R., Giglio, L., Muller, J-P.,  
1708 Lewis, P., Barnsley, M., 1998, The Moderate Resolution Imaging Spectroradiometer  
1709 (MODIS): Land remote sensing for global change research. *IEEE Transactions on*  
1710 *Geoscience and Remote Sensing*. 36. 1228-1249.
- 1711
- 1712 Justice, C. O., Giglio, L., Korontzi, S., Owens, J., Morisette, J. T., Roy, D., Descloitres, J.,  
1713 Alleaume, S., Petitcolin, F., and Kaufman, Y. (2002a) The MODIS fire products. *Remote*  
1714 *Sensing of Environment*. 83. 244-262.
- 1715
- 1716 Justice C.O., Townshend J.R.G., Vermote E.F., Masuoka E., Wolfe R.E., Saleous N., Roy  
1717 D.P., Morisette J. An overview of MODIS land data processing and product status,  
1718 *Remote Sensing of Environment*. 83 (2002b), 3-15.
- 1719
- 1720 Kaiser, J.W., Heil, A., Andreae, M.O., Benedetti, A., Chubarova, N., Jones, L., Morcrette,  
1721 J.J., Razinger, M., Schultz, M.G., Suttie, M., & van der Werf, G.R. (2012). Biomass  
1722 burning emissions estimated with a global fire assimilation system based on observed  
1723 fire radiative power. *Biogeosciences*, 9, 527-554
- 1724
- 1725 Kaufman, Y. J., Tanré, D., and Boucher, O., (2002) A satellite view of aerosols in the  
1726 climate system. *Nature*. 419, no. 6903. 215.
- 1727

- 1728 Kaufman, Y.J., Remer, L.A., Ottmar, R.D., Ward, D.E., Li, R.-R., Kleidman, R., Fraser,  
1729 R.S., Flynn, L., McDougal, D., Shelton, G. (1996). Relationship between remotely sensed  
1730 fire intensity and rate of emission of smoke: SCAR-C experiment. In *Global Biomass*  
1731 *Burning*, edited by J. Levin (Cambridge, MA: The MIT press), pp. 685–696.
- 1732
- 1733 Kaufman, Y.J., Justice, C.O., Flynn, L.P., Kendall, J.D., Prins, E.M., Giglio, L., Ward,  
1734 D.E., Menzel, W.P. and Setzer, A.W. (1998) Potential global fire monitoring from EOS -  
1735 MODIS. *Journal of Geophysical Research: Atmospheres*. 103(D24). 32215-32238.
- 1736
- 1737 Kaufman, Y. J., Tucker, C. J., and Fung, I. (1990), Remote sensing of biomass burning in  
1738 the tropics. *Journal of Geophysical Research*. 95. 9927–9939.
- 1739
- 1740 Kelley, D.I., Burton, C., Huntingford, C., Brown, M.A., Whitley, R. and Dong, N., 2021.  
1741 Low meteorological influence found in 2019 Amazonia fires. *Biogeosciences*, 18(3),  
1742 pp.787-804.
- 1743
- 1744 Korontzi, S., McCarty, J., Loboda, T., Kumar, S., & Justice, C. (2006). Global  
1745 distribution of agricultural fires in croplands from 3 years of Moderate Resolution  
1746 Imaging Spectroradiometer (MODIS) data. *Global Biogeochemical Cycles*. 20. 2.  
1747 <https://doi.org/10.1029/2005GB002529>
- 1748
- 1749 Kremens, R.L., Dickinson, M.B., Bova, A.S. (2012) Radiant flux density, energy density,  
1750 and fuel consumption in mixed-oak forest surface fires. *International Journal of*  
1751 *Wildland Fire*. 21. 722-730. <https://doi.org/10.1071/WF10143>.
- 1752
- 1753 Kumar, S.S. and Roy, D.P. (2018) Global Operational Land Imager (GOLI) Landsat-8  
1754 reflectance based active fire detection algorithm. *International Journal of Digital*  
1755 *Earth*. 11. 2. 154-178.
- 1756

- 1757 Laneve, G., Castronuovo, M.M. and Cadau, E.G. (2006) Continuous monitoring of forest  
1758 fires in the Mediterranean area using MSG. *IEEE Transactions on Geoscience and*  
1759 *Remote Sensing.* 44. 10. 2761-2768.
- 1760
- 1761 Langaas, S. (1992). Temporal and Spatial Distribution of Savanna Fires in Senegal and  
1762 the Gambia, West Africa, 1989-90, Derived From Multi-Temporal AVHRR Night  
1763 Images. *International Journal of Wildland Fire.* 2. 21-36
- 1764
- 1765 Laris, P. (2002) Burning the seasonal mosaic: Preventative burning strategies in the  
1766 wooded savanna of southern Mali. *Human Ecology.* 30. 155-186
- 1767
- 1768 Laurent, P., Mouillot, F., Moreno, M. V., Yue, C. and Cias, P. (2019) Varying  
1769 relationships between fire radiative power and fire size at a global scale. *Biogeosciences.*  
1770 16. 275-288, <https://doi.org/10.5194/bg-16-275-2019>
- 1771
- 1772 Lee, T. F., and Tag, P. M. (1990) Improved detection of hotspots using the AVHRR 3.7  
1773  $\mu\text{m}$  channel. *Bulletin of the American Meteorological Society.* 71. 1722-1730.
- 1774
- 1775 Le Page, Y., Oom, D., Silva, J.M.N., Jonsson, P., & Pereira, J.M.C. (2010). Seasonality of  
1776 vegetation fires as modified by human action: observing the deviation from eco-climatic  
1777 fire regimes. *Global Ecology and Biogeography.* 19. 575-588
- 1778
- 1779 Li, J. and Roy, D.P., 2017, A global analysis of Sentinel-2A, Sentinel-2B and Landsat-8  
1780 data revisit intervals and implications for terrestrial monitoring, *Remote Sensing.* 9(9),  
1781 902.
- 1782
- 1783 Li, F., Zhang, X., Kondragunta, S. and Roy, D. P. (2018) Investigation of the Fire  
1784 Radiative Energy Biomass Combustion Coefficient: A Comparison of Polar and  
1785 Geostationary Satellite Retrievals Over the Conterminous United States. *Journal of*  
1786 *Geophysical Research : Biogeosciences.* <https://doi.org/10.1002/2017JG004279>
- 1787

- 1788 Lu, M., Li, F., Zhan, B., Li, H., Yang, X., Lu, X. and Xiao, H., 2020. An Improved Cloud  
1789 Detection Method for GF-4 Imagery. *Remote Sensing*, 12(9), p.1525.
- 1790
- 1791 Liu, X., He, B., Quan, X., Yebra, M., Qiu, S., Yin, C., Liao, Z. and Zhang, H., 2018. Near  
1792 real-time extracting wildfire spread rate from Himawari-8 satellite data. *Remote*  
1793 *Sensing*, 10(10), p.1654.
- 1794
- 1795 Liu, T., Mickley, L.J., Marlier, M.E., DeFries, R.S., Khan, M.F., Latif, M.T. and  
1796 Karambelas, A., 2020. Diagnosing spatial biases and uncertainties in global fire  
1797 emissions inventories: Indonesia as regional case study. *Remote Sensing of*  
1798 *Environment*, 237, p.111557.
- 1799
- 1800
- 1801 Marchese, F., Mazzeo, G., Filizzola, C., Covello, I., Falconieri, A., Lacava, T., Paciello, R.,  
1802 Pergola, N. and Tramutoli, V. (2017) Issues and Possible Improvements in Winter Fires  
1803 Detection by Satellite Radiances Analysis: Lesson Learned in Two Regions of Northern  
1804 Italy. *IEEE Journal of Selected Topics in Applied Earth Observations and Remote*  
1805 *Sensing*. 10. 7. 3297-3313.
- 1806
- 1807 Mathews, B.J., Strand, E.K., Smith, A.M., Hudak, A.T., Dickinson, B. and Kremens, R.L.  
1808 (2016). Laboratory experiments to estimate interception of infrared radiation by tree  
1809 canopies. *International Journal of Wildland Fire*. 25. 9. 1009-1014.
- 1810
- 1811 Matson, M., and Dozier, J. (1981) Identification of subresolution high temperature  
1812 sources using a thermal IR sensor. *Photogrammetric Engineering and Remote Sensing*,  
1813 47, 1311–1318.
- 1814
- 1815 Matson, M., and Holben, B. (1986). Satellite detection of tropical burning in Brazil.  
1816 *International Journal of Remote Sensing*. 8. 3. 509-516, doi:  
1817 10.1080/01431168708948657.
- 1818

- 1819 Matson, M., Stephens, G., & Robinson, J. (1987). Fire detection using data from the  
1820 NOAA-N satellites. *International Journal of Remote Sensing*. 8. 7. 961-970.
- 1821
- 1822 McLauchlan, K.K., Higuera, P.E., Miesel, J., Rogers, B.M., Schweitzer, J., Shuman, J.K.,  
1823 Tepley, A.J., Varner, J.M., Veblen, T.T., Adalsteinsson, S.A. and Balch, J.K., 2020. Fire  
1824 as a fundamental ecological process: Research advances and frontiers. *Journal of*  
1825 *Ecology*, 108, 2047-2069.
- 1826
- 1827 McCarley, T.R., Hudak, A.T., Sparks, A.M., Vaillant, N.M., Meddens, A.J., Trader, L.,  
1828 Mauro, F., Kreitler, J. and Boschetti, L., 2020. Estimating wildfire fuel consumption  
1829 with multitemporal airborne laser scanning data and demonstrating linkage with  
1830 MODIS-derived fire radiative energy. *Remote Sensing of Environment*, 251, p.112114.
- 1831
- 1832 McCarty, J.L., Korontzi, S., Justice, C.O., & Loboda, T. (2009). The spatial and temporal  
1833 distribution of crop residue burning in the contiguous United States. *Science of the*  
1834 *Total Environment*. 407. 5701-5712
- 1835
- 1836 Morisette, J. T., Giglio, L., Csiszar, I., & Justice, C. O. (2005). Validation of the MODIS  
1837 active fire product over Southern Africa with ASTER data. *International Journal of*  
1838 *Remote Sensing*. 26. 19. 4239-4264.
- 1839
- 1840 Mota, B. and Wooster, M.J. (2018) A new top-down approach for directly estimating  
1841 biomass burning emissions and fuel consumption rates and totals from geostationary  
1842 satellite fire radiative power (FRP). *Remote Sensing of Environment*. 206. 45-62.
- 1843
- 1844 Mouillot, F., Schultz, M. G., Yue, C., Cadule, P., Tansey, K., Ciais, P., & Chuvieco, E.  
1845 (2014). Ten years of global burned area products from spaceborne remote sensing—A  
1846 review: Analysis of user needs and recommendations for future developments.  
1847 *International Journal of Applied Earth Observation and Geoinformation*, 26, 64-79.
- 1848

- 1849 Muirhead, K., and Cracknell, A. P. (1985). Straw burning over Great Britain detected by  
1850 AVHRR. *International Journal of Remote Sensing.* 6, 827-833, doi:  
1851 10.1080/01431168508948506.
- 1852
- 1853 Nguyen, H.M. and Wooster, M.J., 2020. Advances in the estimation of high Spatio-  
1854 temporal resolution pan-African top-down biomass burning emissions made using  
1855 geostationary fire radiative power (FRP) and MAIAC aerosol optical depth (AOD)  
1856 data. *Remote Sensing of Environment*, 248, p.111971.
- 1857
- 1858 Parent, G., Acem, Z., Lechêne, S. and Boulet, P. (2010) Measurement of infrared  
1859 radiation emitted by the flame of a vegetation fire. *International Journal of Thermal  
1860 Sciences*. 49(3). 555-562
- 1861
- 1862 Pastor, E., Àgueda, A., Andrade-Cetto, J., Muñoz, M., Pérez, Y. and Planas, E. (2006)  
1863 Computing the rate of spread of linear flame fronts by thermal image processing. *Fire  
1864 Safety Journal*. 41. 8. 569-579.
- 1865
- 1866 Paugam, R., Wooster, M.J. and Roberts, G. (2012) Use of handheld thermal imager data  
1867 for airborne mapping of fire radiative power and energy and flame front rate of  
1868 spread. *IEEE Transactions on Geoscience and Remote Sensing*. 51. 6. 3385-3399.
- 1869
- 1870 Pereira, M. C., & Setzer, A. W. (1993). Spectral characteristics of fire scars in Landsat-5  
1871 TM images of Amazonia. *International Journal of Remote Sensing*, 14, 2061–2078.
- 1872
- 1873
- 1874 Principe, N.G., & Binford, M.W. (2012). A spatio-temporal analysis of fire recurrence and  
1875 extent for semi-arid savanna ecosystems in southern Africa using moderate-resolution  
1876 satellite imagery. *Journal of Environmental Management*, 100, 72-85
- 1877
- 1878 Prins, E.M. and Menzel, W.P. (1992) Geostationary satellite detection of biomass  
1879 burning in South America. *International Journal of Remote Sensing*. 13. 15.2783-2799.
- 1880

- 1881 Prins, E.M. and Menzel, W.P. (1994) Trends in South American biomass burning  
1882 detected with the GOES visible infrared spin scan radiometer atmospheric sounder from  
1883 1983 to 1991. *Journal of Geophysical Research: Atmospheres*. 99. D8. 16719-16735.
- 1884
- 1885 Prins, E., Feltz, J., Menzel, W., & Ward, D. (1998). An overview of GOES-8 diurnal fire  
1886 and smoke results for SCAR-B and 1995 fire season in South America. *Journal of*  
1887 *Geophysical Research-Atmospheres*, 31821-31835
- 1888
- 1889 Realmuto, V.J., Dennison, P.E., Foote, M., Ramsey, M.S., Wooster, M.J. and Wright, R.,  
1890 2015. Specifying the saturation temperature for the HyspIRI 4- $\mu$ m channel. *Remote*  
1891 *Sensing of Environment*, 167, pp.40-52.
- 1892
- 1893 Reid, J.S., Hyer, E.J., Prins, E.M., Westphal, D.L., Zhang, J., Wang, J., Christopher,  
1894 S.A., Curtis, C.A., Schmidt, C.C., Eleuterio, D.P. and Richardson, K.A. (2009) Global  
1895 monitoring and forecasting of biomass-burning smoke: Description of and lessons from  
1896 the Fire Locating and Modeling of Burning Emissions (FLAMBE) program. *IEEE*  
1897 *Journal of Selecte Topics in Applied Earth Observations and Remote Sensing*, 2. 3. 144-  
1898 162.
- 1899
- 1900 Riggan, P.J., Tissell, R.G., Lockwood, R.N., Brass, J.A., Pereira, J.A.R., Miranda, H.S.,  
1901 Miranda, A.C., Campos, T. and Higgins, R., 2004. Remote measurement of energy and  
1902 carbon flux from wildfires in Brazil. *Ecological Applications*, 14(3), pp.855-872.
- 1903
- 1904 Roberts, G., Wooster, M.J., Perry, G.L., Drake, N., Rebelo, L.M. and Dipotso, F. (2005)  
1905 Retrieval of biomass combustion rates and totals from fire radiative power observations:  
1906 Application to southern Africa using geostationary SEVIRI imagery. *Journal of*  
1907 *Geophysical Research: Atmospheres*. 110. D21.
- 1908
- 1909 Roberts, G. and Wooster. M., J. (2008) Fire Detection and Fire Characterization over  
1910 Africa using Meteosat SEVIRI. *IEEE Transactions on Geoscience and Remote Sensing*.  
1911 48. 4. 1200-1219
- 1912

- 1913 Roberts, G., Wooster, M., and Lagoudakis, E. (2009). Annual and diurnal African  
1914 biomass burning temporal dynamics. *Biogeosciences*, 849-866
- 1915
- 1916 Roberts, G., Wooster, M., Freeborn, P.H., and Xu, W. (2011). Integration of  
1917 geostationary FRP and polar-orbiter burned area datasets for an enhanced biomass  
1918 burning inventory. *Remote Sensing of Environment*. 115. 2047-2061
- 1919
- 1920 Roberts, G. and Wooster, M.J. (2014) Development of a multi-temporal Kalman filter  
1921 approach to geostationary active fire detection & fire radiative power (FRP)  
1922 estimation. *Remote sensing of environment*. 152. 392-412.
- 1923
- 1924 Roberts, G., Wooster, M. J., Xu, W., Freeborn, P. H., Morcrette, J-J., Jones, L.,  
1925 Benedetti, A. and Kaiser, J. (2015) LSA SAF Meteosat FRP Products : Part 2 –  
1926 Evaluation and demonstration of use in the Copernicus Atmosphere Monitoring Service  
1927 (CAMS). *Atmospheric Chemistry and Physics*. 15. 13241-13267.
- 1928
- 1929 Roberts, G., Wooster, M.J., Lauret, N., Gastellu-Etchegorry, J.P., Lynham, T., & McRae,  
1930 D. (2018b). Investigating the impact of overlying vegetation canopy structures on fire  
1931 radiative power (FRP) retrieval through simulation and measurement. *Remote Sensing  
1932 of Environment*. 217. 158-171
- 1933
- 1934 Roberts, G., Wooster, M.J., Xu, W. and He, J., 2018a. Fire activity and fuel consumption  
1935 dynamics in sub-Saharan Africa. *Remote Sensing*, 10(10), p.1591.
- 1936
- 1937 Roberts, G. and Wooster, M.J., 2021. Global impact of landscape fire emissions on  
1938 surface level PM<sub>2.5</sub> concentrations, air quality exposure and population  
1939 mortality. *Atmospheric Environment*, p.118210.
- 1940
- 1941 Roberts, G., Wooster, M.J., Freeborn, P.H. and Xu, W., 2011. Integration of  
1942 geostationary FRP and polar-orbiter burned area datasets for an enhanced biomass  
1943 burning inventory. *Remote Sensing of Environment*, 115(8), pp.2047-2061.
- 1944

- 1945 Rogers, B.M., Balch, J.K., Goetz, S.J., Lehmann, C.E. and Turetsky, M. (2020). Focus on  
1946 changing fire regimes: interactions with climate, ecosystems, and  
1947 society. *Environmental Research Letters*, 15, 30201.
- 1948
- 1949
- 1950 Ross, A.N., Wooster, M.J., Boesch, H. and Parker, R., 2013. First satellite measurements  
1951 of carbon dioxide and methane emission ratios in wildfire plumes. *Geophysical*  
1952 *Research Letters*, 40. 15. 4098-4102.
- 1953
- 1954 Roteta, E., Bastarrika, A., Padilla, M., Storm, T., & Chuvieco, E. (2019). Development of  
1955 a Sentinel-2 burned area algorithm: Generation of a small fire database for sub-Saharan  
1956 Africa. *Remote Sensing of Environment*. 222. 1-17.
- 1957
- 1958 Roy, D.P., Boschetti, L., Justice C.O., Ju, J., (2008), The Collection 5 MODIS Burned  
1959 Area Product - Global Evaluation by Comparison with the MODIS Active Fire Product.  
1960 *Remote Sensing of Environment*.112. 3690-3707.
- 1961
- 1962 Roy, D.P., Huang, H., Boschetti, L., Giglio, L., Yan, L., Zhang, H.K., Li, Z., (2019),  
1963 Landsat-8 and Sentinel-2 burned area mapping - a combined sensor multi-temporal  
1964 change detection approach, *Remote Sensing of Environment*. 231, 111254.
- 1965
- 1966
- 1967 Scholes, R. J., Kendall, J., and Justice, C. O. (1996). The quantity of biomass burned in  
1968 southern Africa. *Journal of Geophysical Research: Atmospheres*. 101. D19., 23667-  
1969 23676.
- 1970
- 1971 Schmit, T. J., Griffith, P., Gunshor, M. M., Daniels, J. M., Goodman, S. J., & Lebair, W.  
1972 J. (2017). A closer look at the ABI on the GOES-R series. *Bulletin of the American*  
1973 *Meteorological Society*, 98(4), 681-698.
- 1974
- 1975

- 1976 Schroeder, W., Prins, E., Giglio, L., Csiszar, I., Schmidt, C., Morisette, J. and Morton, D.,  
1977 2008. Validation of GOES and MODIS active fire detection products using ASTER and  
1978 ETM+ data. *Remote Sensing of Environment*, 112(5), pp.2711-2726.
- 1979
- 1980 Schroeder, W., Oliva, P., Giglio, L., and Csiszar, I. (2014). The new VIIRS 375 m active  
1981 fire detection data product: Algorithm description and initial assessment. *Remote*  
1982 *Sensing of Environment*. 143. 85-96.
- 1983
- 1984 Schroeder, W., P. Oliva, L. Giglio, B. Quayle, E. Lorenz, and F. Morelli. (2016) Active  
1985 Fire Detection Using Landsat-8/OLI Data. *Remote Sensing of Environment*. 185. 210–  
1986 220.
- 1987
- 1988 Seiler. W., and Crutzen, P.J. (1980). Estimates of gross and net fluxes of carbon between  
1989 the biosphere and the atmosphere from biomass burning. *Climate Change*. 2, 207– 248.
- 1990
- 1991 Sembhi, H., Wooster, M., Zhang, T., Sharma, S., Singh, N., Agarwal, S., Boesch, H.,  
1992 Gupta, S., Misra, A., Tripathi, S.N. and Mor, S. (2020). Post-monsoon air quality  
1993 degradation across Northern India: assessing the impact of policy-related shifts in  
1994 timing and amount of crop residue burnt. *Environmental Research Letters*, 15, 104067.
- 1995
- 1996 Setzer, A.W., and Pereira, M.C. (1991). Amazonia biomass burnings n 1987 and an  
1997 estimated of their tropospheric emissions. *Ambio*, 20. 1. 19-22.
- 1998
- 1999 Shephard, M.W. and Kennelly, E.J. (2003) Effect of band-to-band coregistration on fire  
2000 property retrievals. *IEEE Transactions on Geoscience and Remote Sensing*, 41.11.2648–  
2001 2661.
- 2002
- 2003 Smith, A.M.S., & Wooster, M.J. (2005).Remote classification of head and backfire types  
2004 from MODIS fire radiative power and smoke plume observations. *International Journal*  
2005 *of Wildland Fire*. 14. 249-254
- 2006

- 2007 Smith, A. M. S., Tinkham, W. T., Roy, D. P., Boschetti, L., Kremens, R. L., Kumar S. S.,  
2008 Sparks, A. M., Falkowski, M. J., (2013) Quantification of fuel moisture effects on  
2009 biomass consumed derived from fire radiative energy retrievals. *Geophysical Research*  
2010 *Letters*. 40. 23. 6298–6302. doi:10.1002/2013GL058232
- 2011
- 2012 Sofiev, M., Vankevich, R., Lotjonen, M., Prank, M., Petukhov, V., Ermakova, T.,  
2013 Koskinen, J., and Kukkonen, J., 2009. An operational system for the assimilation of the  
2014 satellite information on wild-land fires for the needs of air quality modelling and  
2015 forecasting. *Atmospheric Chemistry and Physics*. 9. 6833-6847, doi:10.5194/acp-9-  
2016 6833-2009.
- 2017
- 2018 Sommers, W.T., Loehman, R.A. and Hardy, C.C., 2014. Wildland fire emissions, carbon,  
2019 and climate: Science overview and knowledge needs. *Forest Ecology and*  
2020 *Management*, 317, pp.1-8.
- 2021
- 2022 Soja, A.J., Sukhinin, A.I., Cahoon, D.R., Shugart, H.H., & Stackhouse, P.W. (2004).  
2023 AVHRR-derived fire frequency, distribution and area burned in Siberia. *International*  
2024 *Journal of Remote Sensing*. 25. 1939-1960
- 2025
- 2026 Sparks, A.M., Kolden, C.A., Smith, A.M., Boschetti, L., Johnson, D.M. and Cochrane,  
2027 M.A. (2018) Fire intensity impacts on post-fire temperate coniferous forest net primary  
2028 productivity. *Biogeosciences*. 15. 4. 1173.
- 2029
- 2030 Sparks, A.M., Smith, A.M., Talhelm, A.F., Kolden, C.A., Yedinak, K.M. and Johnson,  
2031 D.M., (2017) Impacts of fire radiative flux on mature *Pinus ponderosa* growth and  
2032 vulnerability to secondary mortality agents. *International Journal of Wildland Fire*. 26.  
2033 1.95-106.
- 2034
- 2035 Sparks, A.M., Kolden, C.A., Smith, A.M.S., Boschetti, L., Johnson, D.M. and Cochrane,  
2036 M.A. (2018) Fire intensity impacts on post-fire temperate coniferous forest net primary  
2037 productivity. *Biogeosciences*. 15. 4. 1173
- 2038

- 2039 Stott, P. (2000) Combustion in tropical biomass fires: a critical review. *Progress in*  
2040 *Physical Geography*. 24. 3. 355-377.
- 2041
- 2042 Stroppiana, D., Pinnock, S. and Gregoire, J.M. (2000). The global fire product: Daily fire  
2043 occurrence from April 1992 to December 1993 derived from NOAA AVHRR  
2044 data. *International Journal of Remote Sensing*. 21. 6-7. 1279-1288.
- 2045
- 2046 Sullivan, A.L., Ellis, P.F. and Knight, I.K. (2003) A review of radiant heat flux models  
2047 used in bushfire applications. *International Journal of Wildland Fire*. 12. 1. 101-110.
- 2048
- 2049 Trigg, S.N and Roy D.P., 2007, A focus group study of factors that promote and  
2050 constrain the use of satellite derived fire products by resource managers in southern  
2051 Africa, *Journal of Environmental Management*, 82:95-110.
- 2052
- 2053 Udahemuka, G., van den Bergh, F., van Wyk, B. J. and van Wyk, M. A. (2007) Robust  
2054 fitting of the diurnal brightness temperature cycle. *18th Annual Symposium of the*  
2055 *Pattern Recognition Association of South Africa (PRASA)*. Pietermaritzburg, Kwazulu-  
2056 Natal, South Africa. 28-30 November 2007. pp 6.
- 2057
- 2058 van den Bergh, F and Frost, P. E. (2005) A multitemporal approach to fire detection  
2059 using MSG data," in *Proceedings 2nd IEEE International Workshop Analysis Multi-*  
2060 *Temporal Remote Sensing Images*. May 16–18, 2005, pp. 156–160.
- 2061
- 2062 van den Bergh, F., Udahemuka, G., van Wyk, B.J. (2009) Potential fire detection based  
2063 on Kalman-driven change detection. *International Geoscience and Remote Sensing*  
2064 *Symposium. IGARSS 2009*. 12-17 July. Pp 77-80.
- 2065
- 2066 Van der Werf, G.R., Randerson, J.T., Giglio, L., Collatz, G.J., Mu, M., Kasibhatla, P.S.,  
2067 Morton, D.C., DeFries, R.S., Jin, Y.V. and van Leeuwen, T.T., 2010. Global fire  
2068 emissions and the contribution of deforestation, savanna, forest, agricultural, and peat  
2069 fires (1997–2009). *Atmospheric chemistry and physics*, 10(23), pp.11707-11735.
- 2070

- 2071 van der Werf, G.R., Randerson, J.T., Giglio, L., Van Leeuwen, T.T., Chen, Y., Rogers,  
2072 B.M., Mu, M., Van Marle, M.J., Morton, D.C., Collatz, G.J. and Yokelson, R.J., 2017.  
2073 Global fire emissions estimates during 1997–2016. *Earth System Science Data*, 9. 2.  
2074 p.697.
- 2075
- 2076 Veraverbeke, S. and Hook, S.J. (2013) Evaluating spectral indices and spectral mixture  
2077 analysis for assessing fire severity, combustion completeness and carbon  
2078 emissions. *International journal of wildland fire*. 22. 5. 707-720.
- 2079
- 2080 Vermote, E., Ellicott, E., Dubovik, O., Lapyonok, T., Chin, M., Giglio, L. and Roberts,  
2081 G.J., 2009. An approach to estimate global biomass burning emissions of organic and  
2082 black carbon from MODIS fire radiative power. *Journal of Geophysical Research: Atmospheres*, 114(D18).
- 2084
- 2085 Weaver, J.F., Purdom, J.F. and Schneider, T.L. (1995) Observing forest fires with the  
2086 GOES-8, 3.9- $\mu$ m imaging channel. *Weather and Forecasting*, 10. 4.803-808.
- 2087
- 2088 Whitlock, C., Higuera, P.E., McWethy, D.B. and Briles, C.E. (2010) Paleoecological  
2089 perspectives on fire ecology: revisiting the fire-regime concept. *The Open Ecology  
2090 Journal*, 3. 1. 6-23
- 2091
- 2092 Wickramasinghe, C.H., Jones, S., Reinke, K. and Wallace, L. (2016) Development of a  
2093 multi-spatial resolution approach to the surveillance of active fire lines using Himawari-  
2094 8. *Remote Sensing*. 8. 11. 932.
- 2095
- 2096 Wiedinmyer, C., Akagi, S.K., Yokelson, R.J., Emmons, L.K., Al-Saadi, J.A., Orlando, J.J.  
2097 and Soja, A.J., 2011. The Fire INventory from NCAR (FINN): a high resolution global  
2098 model to estimate the emissions from open burning. *Geoscientific Model Development*.  
2099 4. 3. p.625.
- 2100

- 2101 Wooster, M.J. and Rothery, D.A. (1997) Time-series analysis of effusive volcanic activity  
2102 using the ERS along track scanning radiometer: The 1995 eruption of Fernandina  
2103 volcano, Galápagos Islands. *Remote Sensing of Environment*. 62. 1. 109-117.
- 2104
- 2105 Wooster, M. J., Zhukov, B., and Oertel, D., (2003) Fire radiative energy for quantitative  
2106 study of biomass burning: derivation from the BIRD experimental satellite and  
2107 comparison to MODIS fire products. *Remote Sensing of Environment*. 86. 83-107.
- 2108
- 2109 Wooster, M.J., and Zhang, Y.H. (2004). Boreal forest fires burn less intensely in Russia  
2110 than in North America. *Geophysical Research Letters*. 31
- 2111
- 2112 Wooster, M. J., Roberts, G., Perry, G. L. W. and Kaufman, Y. J. (2005) Retrieval of  
2113 biomass combustion rates and totals from fire radiative power observations: FRP  
2114 derivation and calibration relationships between biomass consumption and fire  
2115 radiative energy release. *Journal of Geophysical Research*. 110, D24311.  
2116 doi:10.1029/2005JD006318
- 2117
- 2118 Wooster, M.J., Perry, G.L.W., Zhukov, B. and Oertel, D., 2004. Estimation of energy  
2119 emissions, fireline intensity and biomass consumption in wildland fires: a potential  
2120 approach using remotely sensed fire radiative energy. *Spatial Modeling of the Terrestrial*  
2121 *Environment*, John Wiley & Sons, pp.175-196.
- 2122
- 2123 Wooster, M.J., Perry, G.L.W., & Zoumas, A. (2012a). Fire, drought and El Nino  
2124 relationships on Borneo (Southeast Asia) in the pre-MODIS era (1980-2000).  
2125 *Biogeosciences*, 9, 317-340
- 2126
- 2127 Wooster, M.J., Xu, W. and Nightingale, T. (2012b) Sentinel-3 SLSTR active fire  
2128 detection and FRP product: Pre-launch algorithm development and performance  
2129 evaluation using MODIS and ASTER datasets. *Remote Sensing of Environment*. 120.  
2130 236-254.
- 2131

- 2132 Wooster, M.J., Gaveau, D., Salim, M.A., Zhang, T., Xu, W., Green, D.C., Huijnen, V.,  
2133 Murdiyarso, D., Gunawan, D., Borchard, N. and Schirrmann, M., 2018. New tropical  
2134 peatland gas and particulate emissions factors indicate 2015 Indonesian fires released  
2135 far more particulate matter (but less methane) than current inventories imply. *Remote*  
2136 *Sensing*, 10(4), p.495.
- 2137
- 2138 Wooster, M. J., Roberts, G., Freeborn, P. H., Xu, W., Govaerts, Y., Beeby, R., He, J.,  
2139 Lattanzio, A. and Mullen, R. (2015) Meteosat SEVIRI Fire Radiative Power (FRP)  
2140 products from the Land Surface Analysis Satellite Applications Facility (LSA SAF) – Part  
2141 1 : Algorithms, product contents and analysis. *Atmospheric Chemistry and Physics*. 15.  
2142 9815-9895.
- 2143
- 2144 Xu, W., Wooster, M.J., Roberts, G., & Freeborn, P. (2010). New GOES imager  
2145 algorithms for cloud and active fire detection and fire radiative power assessment across  
2146 North, South and Central America. *Remote Sensing of Environment*. 114. 1876-1895
- 2147
- 2148 Xu, W., Wooster, M.J., Kaneko, T., He, J.P., Zhang, T.R., & Fisher, D. (2017). Major  
2149 advances in geostationary fire radiative power (FRP) retrieval over Asia and Australia  
2150 stemming from use of Himarawi-8 AHI. *Remote Sensing of Environment*. 193, 138-149
- 2151
- 2152 Xu, W., Wooster, M.J., Polehampton, E., Yemelyanova, R. and Zhang, T.R. (2021b).  
2153 Sentinel-3 active fire detection and FRP product performance - impact of scan angle and  
2154 SLSTR middle infrared channel selection, *Remote Sensing of Environment*. In press.
- 2155
- 2156 Xu, W., Wooster, M.J., He, J. and Zhang, T., 2020. First study of Sentinel-3 SLSTR  
2157 active fire detection and FRP retrieval: Night-time algorithm enhancements and global  
2158 intercomparison to MODIS and VIIRS AF products. *Remote Sensing of*  
2159 *Environment*, 248, p.111947.
- 2160
- 2161 Xu, W., Wooster, M.J., He, J. and Zhang, T., 2021a. Improvements in high-temporal  
2162 resolution active fire detection and FRP retrieval over the Americas using GOES-16 ABI

2163 with the geostationary Fire Thermal Anomaly (FTA) algorithm. *Science of Remote*  
2164 *Sensing*, 3, p.100016.

2165

2166 Yang, J., Zhang, Z., Wei, C., Lu, F., & Guo, Q. (2017). Introducing the new generation of  
2167 Chinese geostationary weather satellites, Fengyun-4. *Bulletin of the American*  
2168 *Meteorological Society*, 98(8), 1637-1658.

2169

2170 Yin, L., Du, P., Zhang, M., Liu, M., Xu, T. and Song, Y., 2019. Estimation of emissions  
2171 from biomass burning in China (2003–2017) based on MODIS fire radiative energy  
2172 data. *Biogeosciences*, 16(7), pp.1629-1640.

2173

2174 Zhang, X.S., Kondragunta, S., Ram, J., Schmidt, C., & Huang, H.C. (2012). Near-real-  
2175 time global biomass burning emissions product from geostationary satellite  
2176 constellation. *Journal of Geophysical Research-Atmospheres*. 117. D14.  
2177 doi:10.1029/2012JD017459.

2178

2179 Zhang, F., J. Wang , C. Ichoku, E. Hyer, Z. Yang, C. Ge, S. Su, X. Zhang, S. Kondragunta,  
2180 J. Kaiser, C. Wiedinmyer, and A. da Silva (2014) Sensitivity of mesoscale modeling of  
2181 smoke direct radiative effect to the emission inventory: A case study in northern sub-  
2182 Saharan African region. *Environmental Research Letter*. 9, 075002.

2183

2184 Zhang, X.S., Kondragunta, S., & Roy, D.P. (2014). Interannual variation in biomass  
2185 burning and fire seasonality derived from geostationary satellite data across the  
2186 contiguous United States from 1995 to 2011. *Journal of Geophysical Research-  
2187 Biogeosciences*, 119, 1147-1162

2188

2189 Zhang, T., Wooster, M.J. and Xu, W. (2017) Approaches for synergistically exploiting  
2190 VIIRS I-and M-Band data in regional active fire detection and FRP assessment: A  
2191 demonstration with respect to agricultural residue burning in Eastern China. *Remote*  
2192 *Sensing of Environment*. 198. 407-424.

2193

- 2194 Zhang, T., Wooster, M.J., de Jong, M.C. and Xu, W. (2018) How Well Does the 'Small  
2195 Fire Boost' Methodology Used within the GFED4.1s Fire Emissions Database Represent  
2196 the Timing, Location and Magnitude of Agricultural Burning? *Remote Sensing*, 10. 6.  
2197 823.
- 2198
- 2199 Zhang, T., de Jong, M.C., Wooster, M.J., Xu, W. and Wang, L., 2020. Trends in eastern  
2200 China agricultural fire emissions derived from a combination of geostationary  
2201 (Himawari) and polar (VIIRS) orbiter fire radiative power products. *Atmospheric  
2202 Chemistry and Physics*, 20(17), pp.10687-10705.
- 2203
- 2204 Zhukov, B., Lorenz, E., Oertel, D., Wooster, M. and Roberts, G. (2006) Spaceborne  
2205 detection and characterization of fires during the bi-spectral infrared detection (BIRD)  
2206 experimental small satellite mission (2001–2004). *Remote sensing of  
2207 Environment*, 100. 1. pp.29-51.
- 2208